Coupling model of electromigration and experimental verification – Part I
Effect of atomic concentration gradient

Cui, Zhen; Fan, Xuejun; Zhang, Yaqian; Vollebregt, Sten; Fan, Jiajie; Zhang, Guoqi

DOI
10.1016/j.jmps.2023.105257

Publication date
2023

Document Version
Final published version

Published in
Journal of the Mechanics and Physics of Solids

J. Mech. Phys. Solids 174 (2023) 105257

Contents lists available at ScienceDirect

Journal of the Mechanics and Physics of Solids

journal homepage: www.elsevier.com/locate/jmps

Coupling model of electromigration and experimental verification – Part I: Effect of atomic concentration gradient

Zhen Cui [a], Xuejun Fan [a,b,*], Yaqian Zhang [a], Sten Vollebregt [a], Jiajie Fan [c], Guoqi Zhang [a,*]

[a] Department of Microelectronics, Delft University of Technology, 2628 CD, Delft, the Netherlands
[b] Department of Mechanical Engineering, P.O. Box 10028, Lamar University, Beaumont, TX 77710, USA
[c] Academy for Engineering & Technology, Fudan University, Shanghai 200433, PR China

ARTICLE INFO

Keywords:
Electromigration
Diffusion-induced strain
Molecular dynamics
Threshold product
Critical atomic concentration

ABSTRACT

This paper presented integrated electromigration (EM) studies through experiment, theory, and simulation. First, extensive EM tests were performed using Blech and standard wafer-level electromigration acceleration test (SWEAT)-like structures, which were fabricated on four-inch wafers. Second, a molecular dynamics (MD) simulation-based diffusion-induced strain was incorporated into the existing coupled theory. Third, one-dimensional (1D) governing equations in terms of atomic concentration for un-passivated and passivated configurations were derived for void formation and growth, using a modified Eshelby's solution to consider the effect of passivation. Fourth, a systematic approach was established, including theoretical formulations and experimental methods, to obtain key material properties, i.e., critical atomic concentration and diffusivity. We then determined the material's properties from a specific set of experimental data, using aluminium (Al) as a carrier for demonstration. These properties were then used to predict the time to failure and void growth under various conditions. The theoretical results agreed well with the experimental data. Moreover, we theoretically determined the critical threshold products of current density and conductor length for the un-passivated and passivated configurations, respectively. Both experiment and theory showed that, in the absence of mechanical stress in un-passivated configurations, the atomic self-diffusion, which was opposite to electron wind, was significant in resisting EM development. However, when mechanical stress was present, such as in passivated configurations, stress migration played a dominant role in resisting EM development. Our numerical results showed that the current density exponent n in Black's law remained as 2 in the range of the current density greater than 0.2 MA/cm^2 and rapidly approached infinity at a low level of current density.

1. Introduction

Semiconductor technology is one of the most important innovations in the history of mankind, which has been making profound impacts on human society and every aspect of human life. For decades, electromigration (EM) has always been one of the bottlenecks and a critical reliability concern for the semiconductor industry (Ho and Kwok, 1989; Hu et al., 2018a; Hu et al., 2018b; Hu and

* Corresponding authors.
E-mail addresses: xuejun.fan@lamar.edu (X. Fan), g.q.zhang@tudelft.nl (G. Zhang).

https://doi.org/10.1016/j.jmps.2023.105257
Received 23 November 2022; Received in revised form 13 February 2023; Accepted 27 February 2023
Available online 5 March 2023

Nomenclature

English alphabet

C_a	Atomic concentration
C_{a0}	Initial atomic concentration
$C_{a,critcial}$	Crictial atomic concentration
C_v	Vacancy concentration
C_{v0}	Initial vacancy concentration
C_L	Lattice concentration
Z^*	Effective charge number
e	Elementary charge
k_B	Boltzmann constant
T	Temperature
Q^*	Heat of transport
L	Length
L_c	Critical length
L_p	Characteristic length
V_{drift}	Drift velocity
L_{void}	Void length
f	Vacancy volume relaxation factor
E_c	Elastic Young's modulus of conductor
E_m	Elastic Young's modulus of passivation
t_{total}	Total testing time
$t_{failure}$	Time to EM failure
$\boldsymbol{j}$	Current density
$\boldsymbol{E}$	Electric field
$\boldsymbol{F}$	Body force
$\boldsymbol{I}$	Unit tensor
$\boldsymbol{U}$	Displacement

Greek alphabet

θ	Total volumetric strain
θ^{diff}	Volumetric diffusion-induced strain
$\boldsymbol{\varepsilon}$	Total strain
$\boldsymbol{\varepsilon}^{me}$	Elastic strain
$\boldsymbol{\varepsilon}^{th}$	Thermal strain
$\boldsymbol{\varepsilon}^{diff}$	Diffusion-induced strain
α	Coefficient of thermal expansion
$\boldsymbol{\sigma}$	Mechanical stress
σ_x	Stress in x direction
σ_y	Stress in y direction
σ_z	Stress in z direction
σ	Hydrostatic stress
ρ	Electrical resistivity
Ω	Volume per atom
X	Coefficient of MTF

Parameter combination

φ	E_c/E_m

Luther, 1995; Hu et al., 1999; Suo, 2003; Tu, 2003; Tu et al., 2017). Various EM theories and models have been developed since the 1960s; however, most of them have succeeded only in partially predicting or explaining the complicated phenomena in experiments (Black, 1967, 1969; Clement, 1997; Clement and Thompson, 1995; He et al., 2004; Kirchheim, 1992; Korhonen et al., 1993; Sarychev et al., 1999; Shatzkes and Lloyd, 1986; Sukharev and Zschech, 2004; Sukharev et al., 2007; Yao and Basaran, 2013). Although the industry succeeds in advancing the integrated circuit (IC) technology node every two years, EM solutions have been trial-error and empirical-based, mainly because of its complicated multi-scale and multi-physics nature (Zhang and Roosmalen, 2009; Zhang et al., 2006; Zhang and Roosmalen, 2010). While scaling alone can improve performance for each new silicon technology node, heterogeneous integration using a combination of 3D monolithic and 2.5D/3D advanced packaging technology can boost the system performance significantly with low costs (Dang; et al., 2021; Lau, 2022). Consequently, new EM failures have emerged in redistribution lines

(RDL) and micro-bumps/pillars at the packaging level (Chen et al., 2012; Chen et al., 2010; Dandu and Fan, 2011; Dandu et al., 2010; Liang et al., 2020; Lin et al., 2005). With the "hyper-scaling" of IC to sub-nanoscale and the emerging of quantum computing and photonics technologies, establishing the fundamental understanding of the underlying EM failure mechanisms becomes urgent and vital for the future of micro-/nano- electronics.

EM essentially is an enhanced mass transport process due to momentum transfer between conducting electrons and diffusing metal atoms, which causes the void formation and/or hillock build-up, resulting in an open or short circuit in electronic devices (Kijkanjanapaiboon, 2017; Tan and Roy, 2007; Zhang, 2020). The early study conducted by Black showed that the time to failure due to EM was inversely proportional to the square of current density (Black, 1967, 1969). While EM is primarily induced by high current density, it is not the only driving force at work. The combined balance of other forces, such as mechanical stress migration, atomic self-diffusion, and thermal migration, determines the diffusive motion of atoms (Kirchheim and Kaeber, 1991; Rzepka et al., 1999).

Different theories and models describing EM have evolved over the decades (Blech and Herring, 1976; Blech, 1976; Ceric et al., 2008; Clement and Thompson, 1995; Cui, 2021; Cui et al., 2019, 2020; Kirchheim, 1992; Korhonen et al., 1993; Lin and Basaran, 2005; Pharr et al., 2011; Sarychev et al., 1999; Shatzkes and Lloyd, 1986; Sukharev et al., 2007; Zhang et al., 2012). Blech first presented a steady-state solution considering the counterbalance of atomic flux by a stress gradient against the electrical current (Blech and Herring, 1976; Blech, 1976). The model, however, neglected the effect of self-diffusion and the temperature gradient. Shatzkes and Lloyd constructed a transient-state model that considered the concentration gradient but ignored stress and temperature gradients (Shatzkes and Lloyd, 1986). Kirchheim and Kaeber discovered the importance of a source/sink term in the diffusion equation responsible for the formation and annihilation of vacancies (Kirchheim, 1992). In the models proposed by Korhonen *et al.* (Korhonen et al., 1993) and Clement and Thompson (Clement and Thompson, 1995), transient analytical solutions were obtained for hydrostatic stress and vacancy concentration without considering self-diffusion. It is worth noting that the results were derived under over-constrained conditions (Cui et al., 2019). Subsequently, Sarychev (Sarychev et al., 1999) developed a coupled EM theory using a complex model to describe the diffusion-induced strain. Lin and Basaran (Lin and Basaran, 2005) applied Sarychev's theory and extended it to non-linear viscoplastic time-dependent problems using finite element modelling. Additionally, Sukharev *et al.* (Sukharev et al., 2007) suggested a new equation for diffusion-induced strain and developed analytical solutions for vacancy concentration, atomic concentration, and hydrostatic stress at the steady-state. Ceric *et al.* (Ceric et al., 2008) and Zhang *et al.* (Zhang et al., 2012) used sequentially coupled finite element analysis, without considering the coupling of diffusion-induced strain, to investigate the time-to-failure owing to EM in chips and solder bumps, respectively. Pharr et al. (Pharr et al., 2011) presented a theory that couples creep and EM to calculate the stress distribution in solder joint. Different theories and models described above have yielded inconsistent results and have only been partially verified through experiments.

Various accelerated EM tests have been developed to examine the failure mechanism (Blech, 1998; Blech and Herring, 1976; Blech, 1976; Gan et al., 2001; Lin et al., 2005; Liu, 2017; Ouyang and Kao, 2011; Root and Turner, 1985; Tan and Roy, 2007; Zhang, 2020). Blech *et al.* (Blech, 1976) designed a test structure in which a set of Al lines with different lengths were patterned on a carrier of TiN. In this test structure, both ends of each metal line segment are in perfectly blocking conditions, allowing no atomic flux. This test structure is referred to as "Blech structure". Using the Blech structure, the critical length, known as Blech length, below which the conductor is immune from EM failure, can be determined accordingly. Additionally, the drift velocity, the average velocity of void growth, can also be measured (Blech, 1998). The Blech structure has been used extensively to examine the effect of microstructure and passivation (Blech, 1976; Cho and Thompson, 1989; Lloyd and Smith, 1983; Wada et al., 1987). Another type of EM test structure is either the standard wafer-level EM acceleration test (SWEAT) or the National Institute of Standards and Technology (NIST) test structure (Giroux et al., 1995). In both structures, metal lines are connected to large-area pads at two ends, which serve as reservoirs to constantly provide atomic flux. There are a variety of SWEAT- or NIST- like test structures, such as nano-bridge wires (Jeong et al., 2014; Kozlova et al., 2013). This paper refers to the metal line connected to large pads at the ends as "SWEAT structure". The SWEAT structure has been mainly used to study the Joule heating effect during EM (Giroux et al., 1995; Giroux et al., 1994; Jonggook et al., 1999). However, no studies have been reported using both Blech and SWEAT structures to examine the underlying EM failure mechanism.

The EM-induced void formation has been attributed to mechanical failure caused by hydrostatic stress or its gradient. Therefore, hydrostatic stress was commonly considered as a failure criterion for EM (Blech, 1976; Gleixner et al., 1997; He et al., 2004; Kirchheim, 1992; Korhonen et al., 1993; Lloyd, 1982; Lloyd and Smith, 1983; Sukharev et al., 2007). The exact critical hydrostatic stress, however, has not been determined. The theoretical study by Gleixner *et al.* showed that the required hydrostatic stress for void formation depends on many factors, such as vacancy concentration, defect types, and location (Gleixner et al., 1997). The results of Korhonen *et al.* (Korhonen et al., 1993) showed that the maximum hydrostatic stress could reach around 500 MPa and compared the predicted stress with the measurement by Hemmert *et al.* (Hemmert and Costa, 1991). The results of Kirchheim *et al.*, He *et al.*, and Sukharev *et al.* predicted the maximum hydrostatic stress at the steady-state in the range of 200 – 500 MPa (He et al., 2004; Kirchheim, 1992; Sukharev et al., 2007). However, Lin *et al.* (Lin and Basaran, 2005) and Cui *et al.* (Cui et al. 2019) predicted the hydrostatic stress at a low range of 20 – 100 MPa. On the other hand, numerous studies showed that EM developed more rapidly in un-passivated metal lines than that with passivation. (Blech, 1976; Lloyd, 1982; Lloyd and Smith, 1983). But in an un-passivated configuration, the hydrostatic stress is less significant owing to the lack of constraints. This means that hydrostatic stress or its gradient may not play a dominant role in EM under certain conditions.

Some studies suggested using vacancy or atomic concentration as a failure criterion for EM as they are directly related to void formation (Clement, 1992; Clement, 1997; Cui et al., 2019; Lloyd, 1999; Shatzkes and Lloyd, 1986). The predicted vacancy concentration, however, was only in the range of 2 - 4 times the initial vacancy concentration for most of the models in the literature (Clement and Thompson, 1995; Shatzkes and Lloyd, 1986; Sukharev et al., 2007). These results implied that when voids are formed,

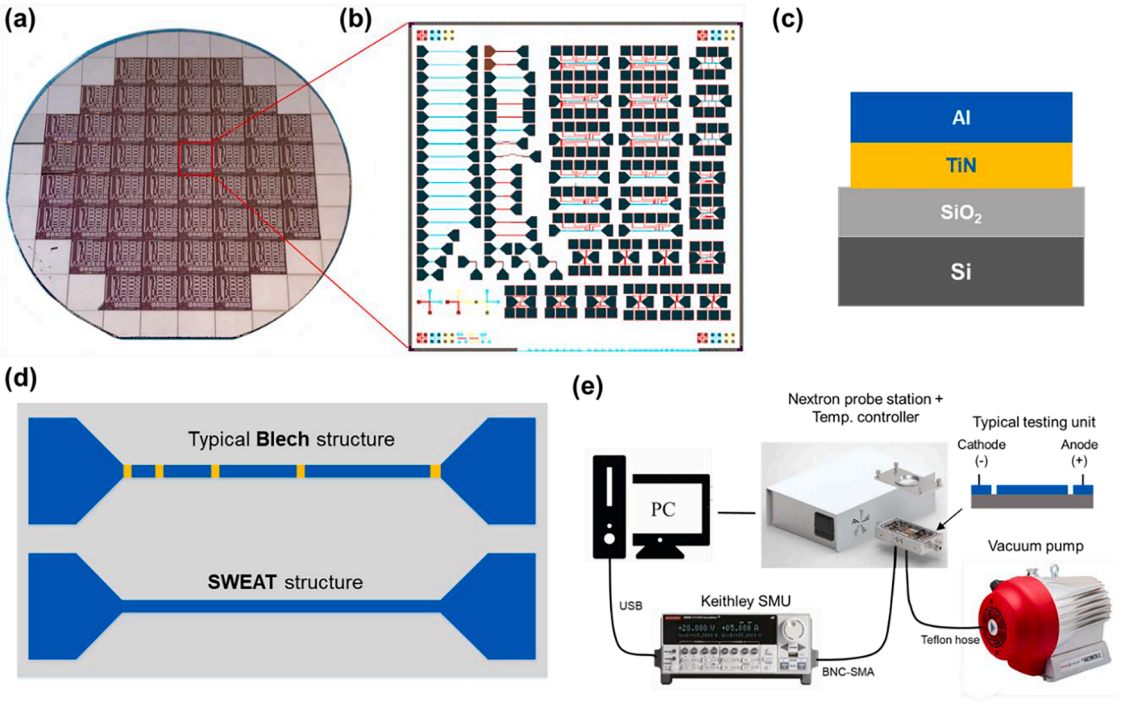

Fig. 1. (a) A 4-inch wafer containing 52 dies. (b) The layout of 63 EM test specimens in each die. (c) Schematic for the cross-section of layer stacks. (d) Schematic of Blech and SWEAT structures. (e) Schematic of EM measurement platform.

only two to four vacancies are created per million atoms, which is nowhere near enough to induce void formation. The vacancy concentration remained around twice the initial vacancy concentration even after a coupling model was developed (Cui et al., 2019).

This paper aims to present a comprehensive electromigration (EM) study through experiment, theory, and simulation. First, various EM test specimens were designed and fabricated with different geometries and structures using Al as a carrier. Both Blech and SWEAT structures were applied and tested for comparison. The effects of annealing and passivation were investigated. Second, we introduced a three-dimensional (3D) coupled EM theory that incorporates a new stress-strain constitutive equation. An equation of diffusion-induced strain in the constitutive equation was based on molecular dynamics (MD) simulations (Cui et al., 2021). Furthermore, analytical one-dimensional (1D) governing equations were derived for un-passivated and passivated configurations, respectively. Moreover, a model for void growth in the Blech structure was developed. Consequently, the critical atomic concentration and diffusivity were determined from both theory and experiments. Subsequently, the numerical results were presented and compared extensively with the experimental data, not only for void formation but also for void growth. We further discussed the critical threshold product of the current density and conductor length under un-passivated and passivated conditions. We also discussed the current density exponent n, introduced by Black. Finally, we established a general design rule against EM failure and presented conclusions and the perspectives.

2. Experiment

Fig. 1 illustrated the schematic of the EM test wafer (Fig. 1(a)), test units on a die (Fig. 1(b)), a cross-section of the layer-stack (Fig. 1(c)), Blech, and SWEAT structures (Fig. 1(d)), and the EM test platform (Fig. 1(e)). EM test specimens were fabricated on 4-inch silicon wafers. A full EM test wafer consisted of 52 dies, each having 63 test specimens. The silicon dioxide layer was deposited using thermal oxidation on the silicon surface because the oxidation layer performs a good adhesion to silicon and also provides excellent electrical isolation. The thin TiN film was then deposited using reactive sputtering at 350°C and patterned using photolithography and reactive ion etching. TiN acted as a conductor and as a barrier layer to avoid atomic diffusion between the dioxide surface and the metal on the top. In this study, sputtered Al stripes with different geometries and structures were patterned by a combination of lithography and wet etching on the TiN layer. Since Al has much better conductivity than TiN, the electrical current mostly flows through the Al stripe. Both Blech and SWEAT structures were designed and fabricated. In a Blech structure specimen, a single metal stripe can include different lengths with spaces. A SWEAT structure has two ends connected to large pads.

The width and thickness of Al specimens were 5 μm and 200 nm, respectively, unless otherwise noticed in this study. During the EM test, a temperature of 250 °C and an electrical current density of 1 MA/cm^2 were applied. All measurements were performed in the vacuum condition in order to prevent undesired oxidation.

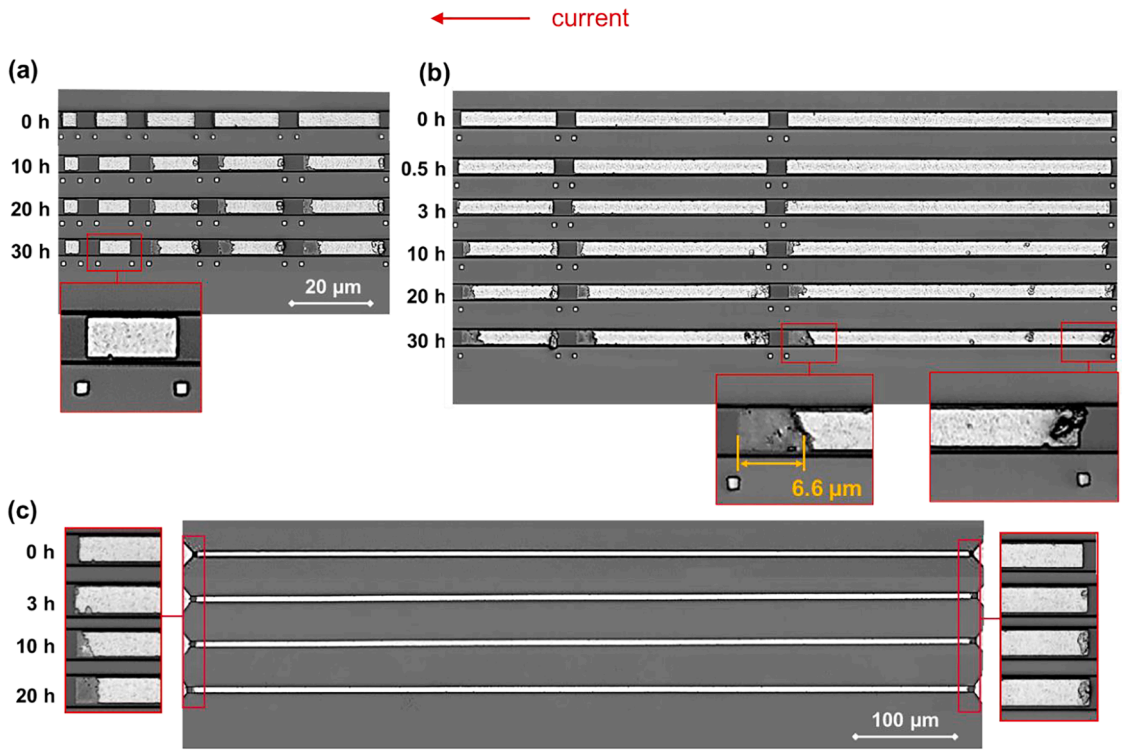

Fig. 2. Optical images of different geometries of Blech structure at various time intervals under the current density of 1 MA/cm^2 and temperature of 250 °C (non-annealing). (a) Images of 5/10/15/20/25 μm Al lines at 0/10/20/30 h. (b) Images of 30/60/100 μm Al lines at 0/0.5/5/10/20/30 h. (c) Images of an 800 μm Al line at 0/3/10/20 h. The width and thickness of all conductors are 5 μm and 200 nm, respectively. The electrical current moved from right to left.

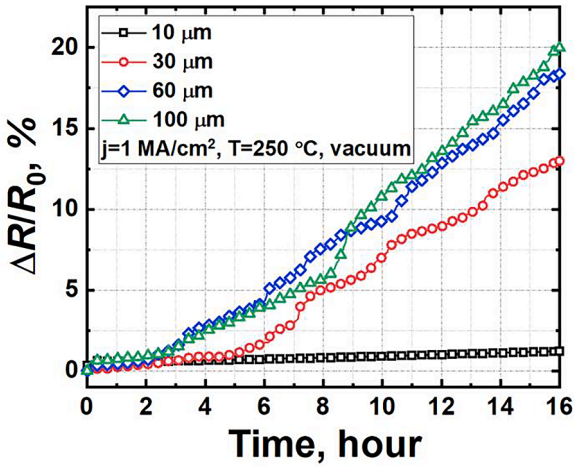

Fig. 3. Changes in resistance for 10/30/60/100 μm Al lines under 1 MA/cm^2 at 250°C.

2.1. Various lengths

Al lines ranging from 5 to 800 μm were tested in 9 lengths. Three geometries of Blech structures: five lengths of 5/10/15/20/25 μm on a stripe; three lengths of 30/60/100 μm on a stripe; and a single-length stripe with 800 μm were used. The EM test duration was up to 30 h. Each specimen was removed from the test chamber at various time intervals during the test for optical inspection using a laser scanning microscope. Each geometry was tested multiple times for repeatability and consistency checks. Fig. 2 shows the optical images of different specimens at different time intervals. Since both ends of each metal line were in perfectly blocking conditions with no atomic flux, voids were formed and grown at the cathode side, and hillocks were formed near the anode side. Al lines with lengths of

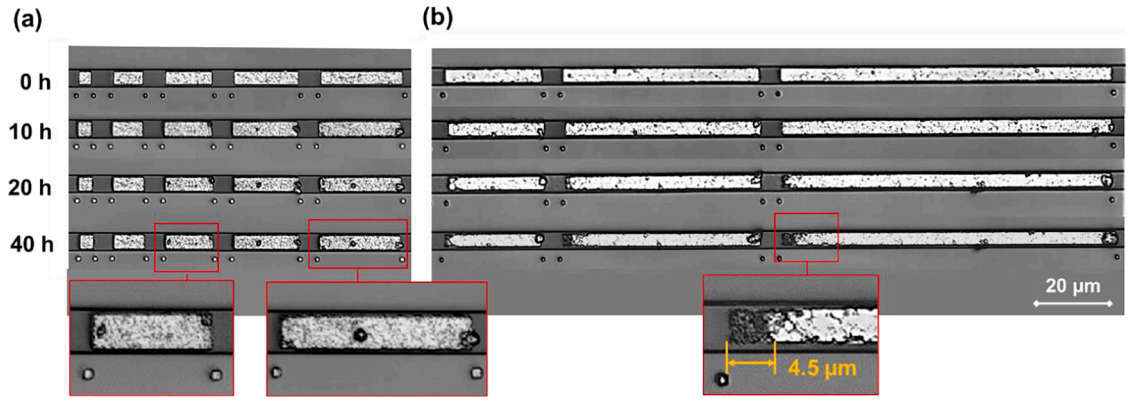

Fig. 4. Optical images of different geometries of Blech structure at various time intervals under the current density of 1 MA/cm^2 and temperature of 250 °C (with annealing). (a) Optical images of 5/10/15/20/25 μm Al lines at 0/10/20/40 h. (b) Optical images of the 30/60/100 μm Al lines at 0/10/20/40 h. The width and thickness of all conductors were 5 μm and 200 nm, respectively. The electrical current moved from right to left.

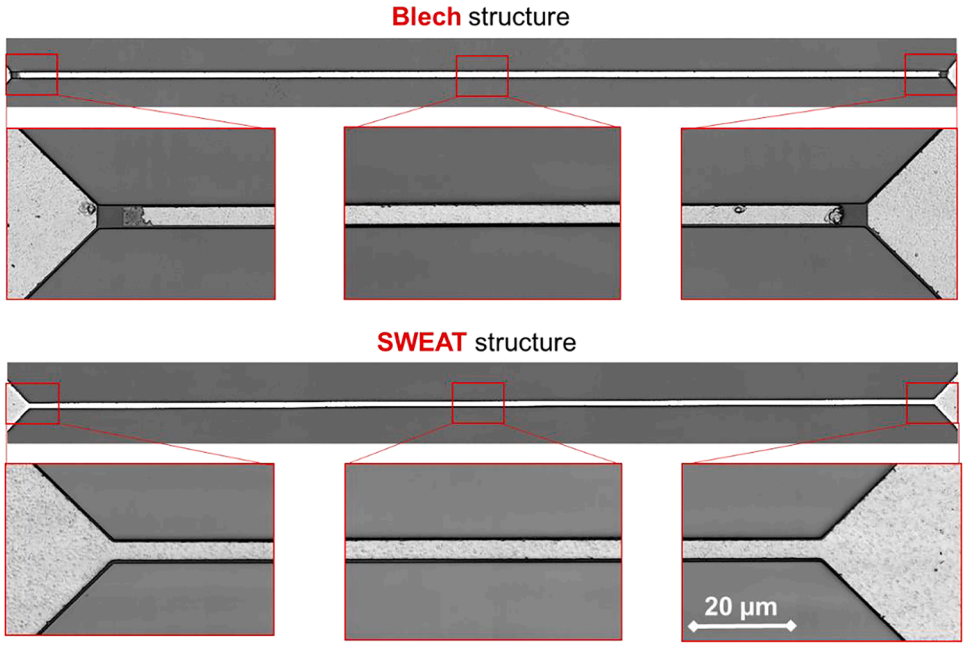

Fig. 5. Comparison of experimental results for Blech versus SWEAT structures at 10 h for 800 μm length (no annealing). No damage was observed in the SWEAT structure and in the mid-section of Blech structure. The applied electrical current density was 1 MA/cm^2 flowing from right to left, and the temperature was 250 °C. The width and thickness of the conductors were 5 μm and 200 nm, respectively.

30/60/100 μm began to form voids at approximately 30 min. However, even after 30 h, no voids and hillocks were observed in the 5 and 10 μm lines. Furthermore, the void lengths at 10 h and 20 h in the 800 μm line were similar to those in the 100 μm line.

Fig. 3 showed the change in resistance for the lengths of 10/30/60/100 μm. For the 10 μm length, the resistance did not change significantly. The critical length was then determined as approximately 10 μm. For the 30/60/100 μm lengths, the resistance continually increased with time, but the difference in the resistance between 60 μm and 100 μm was not significant, indicating a similar EM development in the 60 μm to 100 μm lines. This was consistent with the void growth shown in Fig. 2.

Blech *et al.* introduced the average drift velocity, V_{drift}, to describe the velocity of void growth (Blech, 1998),

$$V_{\text{drift}} = \frac{L_{\text{void}}}{t} \tag{1}$$

where L_{void} is the void length, and t is the time duration. For the 100 μm Al film, its average drift velocity was determined to be 0.0608 ± 0.005 nm/s. The critical length and drift velocity were used in the subsequent section to determine the critical atomic concentration and diffusivity.

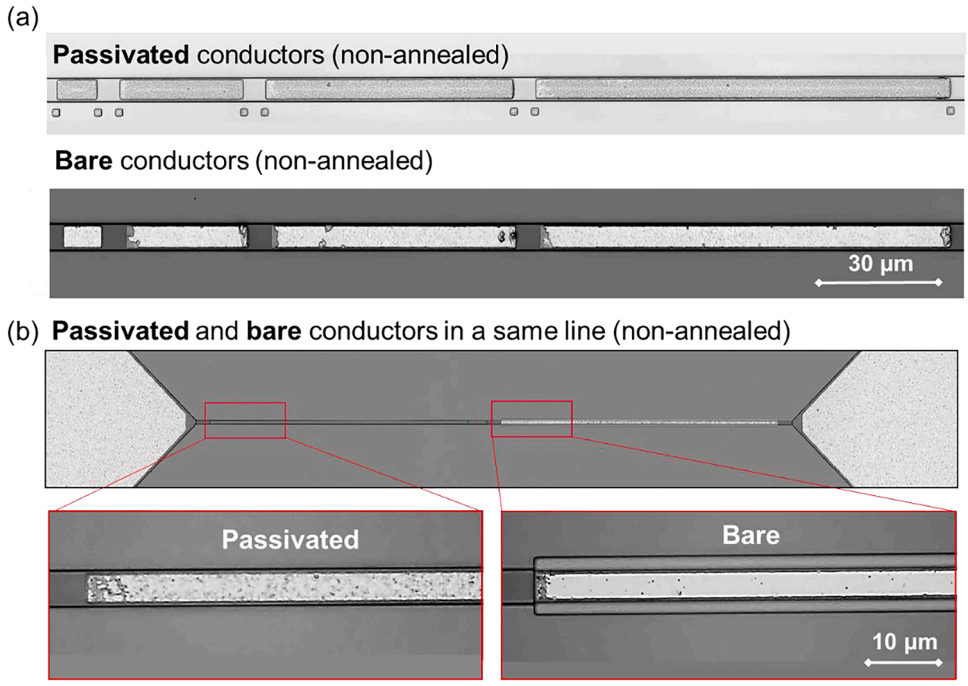

Fig. 6. Comparison of EM development using Blech structure with and without passivation for non-annealed Al under a current density of 1 MA/cm^2 and temperature of 250 °C. (a) Optical images of the passivated and bare Al specimens with different lengths of 10/30/60/100 μm at 10 h. (b) Optical image of a specimen consisting of both bare and passivated conductors of 200 μm length for each at 10 h. The width and thickness of the conductors are 5 μm and 200 nm, respectively.

Furthermore, some wafers were annealed at 450 °C for 30 min in a vacuum chamber, and then tested under 1 MA/cm^2 at 250 °C. Fig. 4 showed the EM results of two geometries in 8 lengths for the annealed Al specimens. As expected, the EM development in the annealed Al occurred later than that in non-annealed Al, indicating a slower EM progress. The drift velocity in the annealed 100 μm Al line was found to be 0.0313 ± 0.003 nm/s, almost half of that in a non-annealed line. The critical length after annealing was approximately 15 μm. Several studies have shown that annealing could reduce the defect density in metals and balance the grain boundary energy via recrystallization or grain growth (Rangaraju et al., 2005; Rao et al., 2013; Tong et al., 2015; Volin and Balluffi, 1968).

2.2. *Blech vs. SWEAT structure*

Fig. 5 showed the optical images of the specimens with Blech and SWEAT structures (no annealing) for 800 μm length at 10 h under the current density of 1 MA/cm^2 and temperature of 250 °C. No voids/hillocks were observed along the length except the two ends in Blech structure. However, there was no damage observed in the entire length of the SWEAT structure. This does not mean that EM did not occur in the SWEAT structure. Instead, the large pad on the cathode acted as a reservoir providing a constant atomic concentration so that the atomic concentration remained constant along the length. On the other hand, the undamaged SWEAT structure implied that the temperature gradient due to Joule heating was insignificant under the current density of 1 MA/cm^2. After increasing current density, different experimental results for the SWEAT structures were observed, which were discussed separately in the second part of this work (Cui et al., 2023).

2.3. *Effect of mechanical stress*

To study the effect of mechanical stress, a 900 nm-thick Si_3N_4 film was deposited using plasma-enhanced chemical vapor deposition at 400°C on Al as a passivation layer. First, the specimens without annealing were tested. As shown in Fig. 6(a), the passivation layer did not reduce the EM development compared to the bare stripe with lengths of 10/30/60/100 μm at 10 h. To further confirm this phenomenon, a specimen consisting of both bare and passivated conductors, each with 200 μm length, were tested simultaneously, as shown in the optical images at 10 h in Fig. 6(b). The voids growth in the passivated conductor was even greater than that in the bare conductor. For the Al without annealing, there were plenty of defects, e.g., point defects in lattice and line defects at the grain boundary area (Rangaraju et al., 2005). Therefore, the grains in the non-annealed Al were not tightly arranged due to those defects. Consequently, no much mechanical stress was generated during EM, even after passivation.

Next, the specimens with annealing were tested. We tested the passivated and un-passivated stripes with lengths of 10/30/60/100/

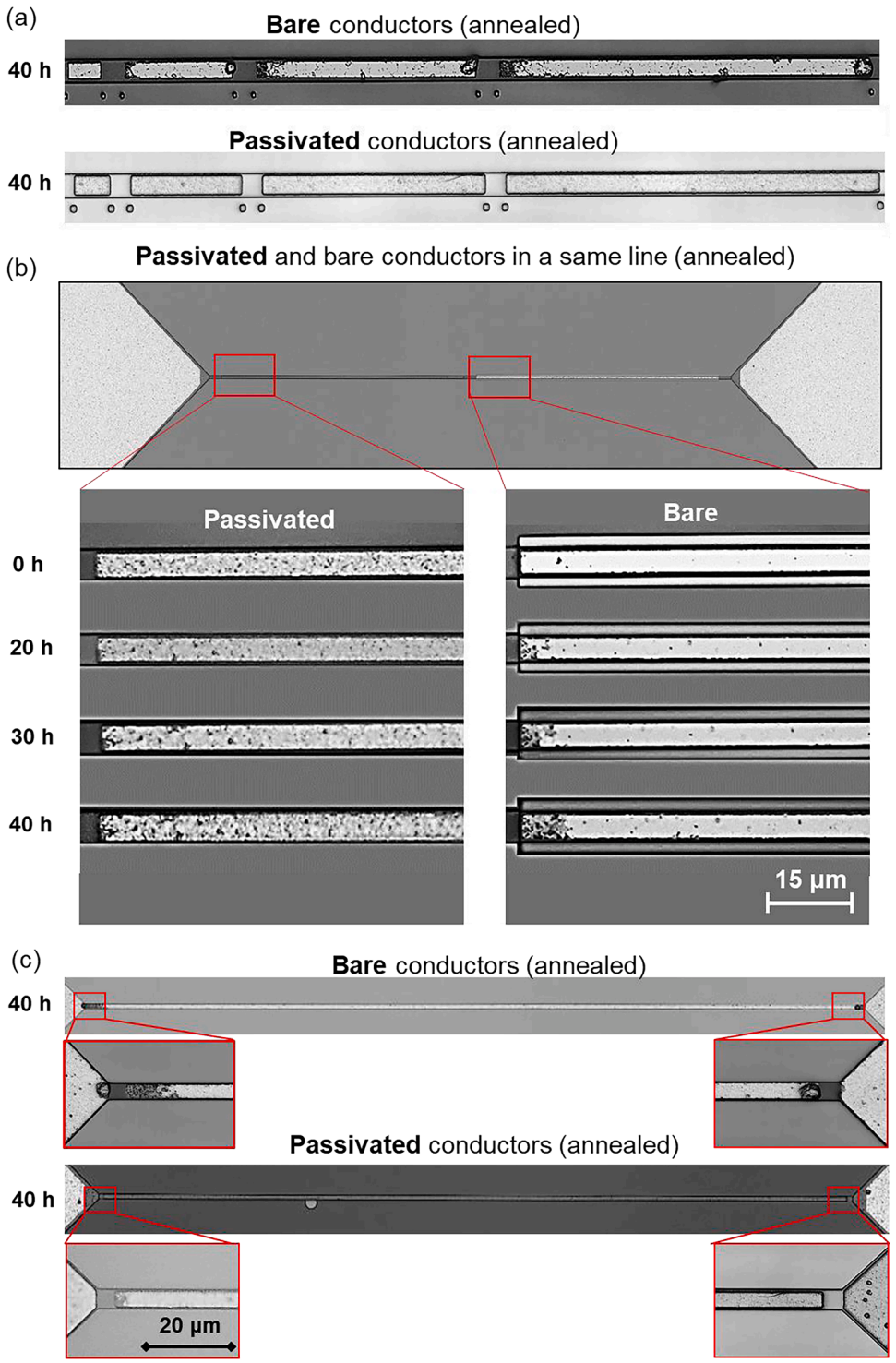

Fig. 7. (a) Optical images of the passivated and bare Al specimens with different lengths of 10/30/60/100 μm at 40 h. (b) Optical images of the specimens consisting of both bare and passivated conductors of 200 μm length for each with the Blech structure. The current density was 1 MA/cm^2, and the temperature was 250 °C. (c) Optical images for 800 μm passivated and bare Al specimens after 40 h tests.

200/800 μm, as shown in Fig. 7. As plotted in Fig. 7(a), no voids were observed in 10/30/60/100 μm conductors after 40 hours. Compared to the un-passivated conductors, we could see that the passivation slowed down the EM damage significantly. Fig. 7(b) plotted the results at various time intervals in 200 μm Al stripes with and without passivation. It can be seen that the development of

EM in passivated conductor was much slower than that in the bare conductor. Moreover, Fig. 7(c) showed that after 40 hours, the void size in passivated 800 μm Al stripe is obviously smaller than that in the un-passivated 800 μm Al stripe. Those results indicated that mechanical stress played an important role in annealed Al conductors with passivation. For thin metal films, it was believed that the annealing process could reduce defects (Rangaraju et al., 2005; Rao et al., 2013; Zhu et al., 2014) and promote the coalescence between grains (Zhou et al., 2019). Thus, the microstructure in annealed Al conductor was tightly arranged, which enables mechanical stress generation in the passivated conductor during EM.

Blech *et al.*, Proost *et al.,* and Hu *et al.* conducted the EM tests in Al interconnects using Blech structures (Blech, 1976; Hu et al., 1993; Proost et al., 2002). Proost *et al.* determined the critical length for Al without annealing was 10.2±0.2 μm under a current density of 1 MA/cm^2 at temperatures from 155 to 230 °C (Proost et al., 2002). Blech *et al.* (Blech, 1976) obtained that the threshold product of current density and conductor length in the annealed Al lines ranged from 1400 to 2000 A/cm at 250 °C. Our tests above showed that the critical length for annealed Al was 15 μm under 1 MA/cm^2 at 250 °C, which corresponded to the threshold product of 1500 A/cm. For the passivated Al lines, Blech *et al.* determined the threshold product around 4600 A/cm at a much higher temperature of 350 °C. We observed that under a current density of 1 MA/cm^2 at temperatures of 250 °C, there were no voids for conductors with lengths from 10 to 100 μm, but there was slight EM failure for the conductor with a length of 200 μm. Thus, the critical threshold product for the passivated Al was between 10,000 A/cm and 20,000 A/cm at 250 °C, according to our experiment.

3. Theory

Atomic transport in EM is caused by a combination of interacting driving/resistive forces arising from different physical causes, such as the gradient of atomic concentration, momentum exchange with current carriers (electron wind), temperature gradient, and mechanical stress gradient (Cui et al., 2019; Kirchheim and Kaeber, 1991; Sukharev and Zschech, 2004; Sukharev et al., 2007). These gradients are responsible for self-diffusion, EM, thermomigration, and stress-induced migration. Thus, EM is essentially a coupled multi-physics problem. The total atomic flux, $\boldsymbol{J}_a$, generally is written as

$$\boldsymbol{J}_a = D_a\left(-\nabla C_a - C_a\frac{Z^* e\rho \boldsymbol{j}}{k_B T} + C_a\frac{\Omega\nabla\sigma}{k_B T} - C_a\frac{Q^*\nabla T}{k_B T^2}\right) \tag{2}$$

where C_a is the atomic concentration (m^{-3}), D_a is the atomic diffusivity(m^2/s), Z^* is the effective charge number ($Z^*>0$), e is the elementary charge (C), ρ is the electrical resistivity (Ohm•m), $\boldsymbol{j}$ is the current density vector (A/m^2), k_B is the Boltzmann constant (J/K), Ω is the volume per atom (m^3), T is the temperature (K), σ is the hydrostatic stress (N/m^2), $\sigma = tr(\boldsymbol{\sigma})/3$, and Q^* is the heat of transport (J/mol). Eq. (2) contains all driving/resistive forces for atomic transport, namely, the diffusional term by the gradient of the atomic concentration, the EM itself, and the forces due to gradients of temperature and mechanical stress.

The atomic transport in EM must be solved concurrently with the governing equations of the stress, displacement-strain, electric, and temperature fields. These equations are given as follows (Cui, 2021; Cui et al., 2019),

$$\frac{\partial\theta}{\partial t} = -\Omega\nabla\cdot\boldsymbol{J}_a \tag{3}$$

$$\theta = tr(\boldsymbol{\varepsilon}) \tag{4}$$

$$\boldsymbol{\varepsilon} = \boldsymbol{\varepsilon}^{\mathrm{me}} + \boldsymbol{\varepsilon}^{\mathrm{th}} + \boldsymbol{\varepsilon}^{\mathrm{diff}} \tag{5}$$

$$d\boldsymbol{\varepsilon}^{\mathrm{th}} = \alpha dT\boldsymbol{I} \tag{6}$$

$$\boldsymbol{\sigma} = \lambda tr(\boldsymbol{\varepsilon}^{\mathrm{me}})\boldsymbol{I} + 2G\boldsymbol{\varepsilon}^{\mathrm{me}} \tag{7}$$

$$\sigma = tr(\boldsymbol{\sigma})/3 \tag{8}$$

$$\nabla\cdot\boldsymbol{\sigma} + \boldsymbol{F} = 0 \tag{9}$$

$$\boldsymbol{\varepsilon} = \frac{1}{2}(\nabla\boldsymbol{u} + \boldsymbol{u}\nabla) \tag{10}$$

$$\nabla\cdot\boldsymbol{j} = 0 \tag{11}$$

$$\boldsymbol{j} = \frac{\boldsymbol{E}}{\rho} \tag{12}$$

$$k\nabla^2 T + \boldsymbol{j}\cdot\boldsymbol{E} = 0 \tag{13}$$

where θ is the total volumetric strain, $\boldsymbol{\varepsilon}$ is the total strain, $\boldsymbol{\varepsilon}^{\mathrm{me}}$ the elastic strain, $\boldsymbol{\varepsilon}^{\mathrm{th}}$ the thermal strain, $\boldsymbol{\varepsilon}^{\mathrm{diff}}$ is the diffusion-induced strain, α is the coefficient of thermal expansion, $\boldsymbol{I}$ is the unit tensor, G and λ are lamé constants $2G=E/(1+\nu)$ and $\lambda=2G\nu/(1-2\nu)$, E is the Young's modulus, ν is the Poisson's ratio, $\boldsymbol{F}$ is the body force (N), $\boldsymbol{u}$ is the displacement (m), $\boldsymbol{E}$ is the electric field (V/m), and k is

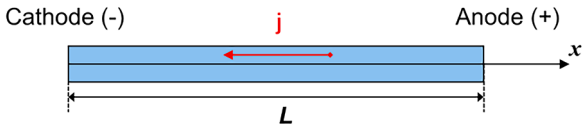

Fig. 8. Schematic of 1D EM problem where atomic concentration $C_a(x,t)$ and hydrostatic stress $\sigma(x,t)$ are the two unknowns.

the thermal conductivity (W•K^{-1}).

Eq. (3) is a mass conservation equation in terms of the total atomic flux ($\boldsymbol{J}_a$) and volumetric strain (θ), which was introduced by He et al. He et al., 2004) and Tan et al. (Tan and Roy, 2007). As discussed in reference (Cui et al., 2019), Eq. (3) naturally includes the source/sink term to account for the formation and annihilation of vacancies in EM development. Linear elastic stress-strain relationship is applied in Eq. (7), which is coupled with thermal and diffusion-induced strain (Eqs. (5) and ((6)). Diffusion-induced strain, $\boldsymbol{\varepsilon}^{\text{diff}}$, for substitutional diffusion, which is dominant in grain boundary diffusion in Al, was described as follows (Garikipati et al., 2001; Sukharev et al., 2007),

$$d\theta^{\text{diff}} = (1-f)\frac{dC_a}{C_a} \tag{14}$$

where f is the vacancy volume relaxation factor that varies between 0 and 1, i.e., $0 < f < 1$. Through large-scale MD simulation, vacancy concentration-dependent f was determined in a wide range of atomic concentrations (Cui et al., 2021). According to the MD results, an empirical equation for f at various concentrations was written as follows (Cui et al., 2021),

$$f(C_a) = \begin{cases} f_0, \ 0.9925 \le \dfrac{C_a}{C_{a0}} \le 1.0025 \\ A\exp\left[B\left(1-\dfrac{C_a}{C_{a0}}\right)\right], \ \text{else} \end{cases} \tag{15}$$

where C_{a0} is the initial atomic concentration, $C_{a0} \approx 1/\Omega$. f_0=0.73, A=1.08, and B=-55.30 for Al. Li *et al.* (Li et al., 2009) also used MD simulation to determine f in Al, but the model contained only ~1000 atoms. As a result, a much higher value of f was obtained.

Eqs. (3) to (15) provide a complete set of equations for coupled 3D analysis. Of these equations, only the atomic transport equation takes time-dependent processes into account, while the other fields are considered quasi-static. This is because the time scale of the EM process is much longer compared to the temperature, electric and stress fields.

The atomic concentration C_a is related to the vacancy concentration C_v as follows,

$$C_a + C_v = C_{a0} + C_{v0} = C_L \tag{16}$$

where C_{v0} is the initial vacancy concentration, and C_L is the lattice site concentration, $C_L = 1/\Omega$. If $C_{v0} \approx 10^{-6} C_{a0}$ (Korhonen et al., 1993), we have

$$\frac{C_v}{C_{v0}} \approx \left(1-\frac{C_a}{C_{a0}}\right)10^6 \tag{17}$$

Let us consider a one-dimensional (1D) problem where all field variables depend only on x and t, as shown in Fig. 8. The effect of joule heating was neglected in this study under the given current density, according to the experimental results. Furthermore, a constant current density -j was applied. Then, the above equations for the atomic flux J_a, the hydrostatic stress σ, and the equilibrium were simplified as follows,

$$J_a = D_a\left(-\frac{\partial C_a}{\partial x} - \frac{C_a}{k_B T} Z^* e\rho j + \frac{C_a}{k_B T}\frac{\Omega \partial \sigma}{\partial x}\right) \tag{18}$$

$$\sigma = \frac{1}{3}\left(\sigma_x + \sigma_y + \sigma_z\right) \tag{19}$$

$$\frac{\partial \sigma_x}{\partial x} = 0 \tag{20}$$

where atomic concentration $C_a(x,t)$ and hydrostatic stress $\sigma(x,t)$ were the only two field variables to be solved. Eq. (20) indicated that σ_x remains a time-dependent constant along the length to satisfy the equilibrium, while the hydrostatic stress σ varies with x to produce a gradient. However, 3D stress-strain equations (Eqs. (4) – (7)) must be applied to determine the hydrostatic stress σ that depends on three stress components, as shown in Eq. (19).

For Blech structures, where no atomic flux is allowed at both ends, the boundary conditions are

$$J_a(0,t) = J_a(L,t) = 0 \tag{21}$$

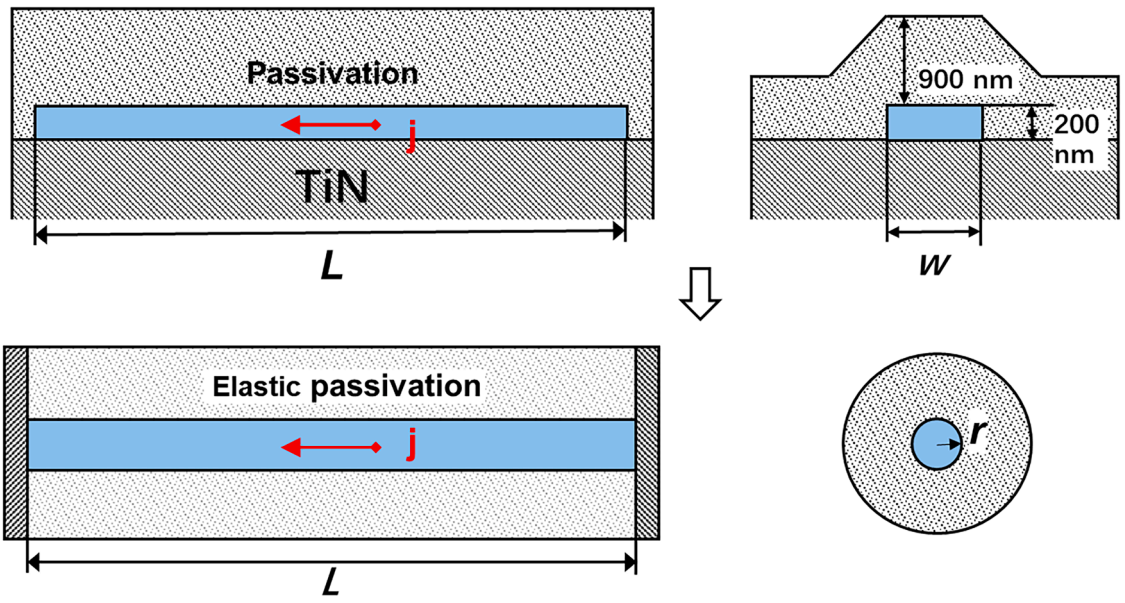

Fig. 9. Schematic of the elastically-passivated configuration. The conductor was idealized as a cylindrical shape, passivated by an elastic material.

For the SWEAT structures, atomic concentration maintains constant due to the connections to the pads; thus, the boundary conditions are

$$C_a(0,t) = C_a(L,t) = C_{a0} \tag{22}$$

For both structures, the initial condition is

$$C_a(x,0) = C_{a0} \tag{23}$$

3.1. Governing equation for un-passivated configuration

Assuming that all stress components are zero in the un-passivated conductor, Eq. (3) finally became,

$$\frac{1-f(C_a)}{C_a}\frac{\partial C_a}{\partial t} = D_a\left(-\frac{Z^* e\rho j}{k_B T}\frac{\partial C_a}{\partial x} + \frac{\partial^2 C_a}{\partial x^2}\right) \tag{24}$$

For a Blech structure, the above equation was solved numerically with the initial condition (Eq. (23)) and following boundary conditions,

$$J_a(0,t) = \frac{Z^* e\rho j}{k_B T}C_a(0,t) - \frac{\partial C_a(0,t)}{\partial x} = 0 \tag{25}$$

$$J_a(L,t) = \frac{Z^* e\rho j}{k_B T}C_a(L,t) - \frac{\partial C_a(L,t)}{\partial x} = 0 \tag{26}$$

For a SWEAT structure, with the boundary conditions of Eq. (22), the solution of Eq. (24) is,

$$C_a(x,t) = C_{a0} \tag{27}$$

$$J_a(x,t) = -\frac{D_a C_{a0}}{k_B T}Z^* e\rho j \tag{28}$$

which means that a constant atomic concentration remains all time for the entire metal line. This was in agreement with the experimental results shown in the previous section. Eq. (28) implied that the atomic flux maintains a constant, indicating atomic transport continually progressing in the conductor, despite that there is no damage in SWEAT structures.

3.2. Governing equation for elastically-passivated configuration

For passivated configurations, to obtain an approximate solution, the conductor line was idealized as a cylindrical shape, shown in Fig. 9. The cylinder was laterally passivated by elastic material, and both ends of the conductor were constrained.

Atomic concentration $C_a(x,t)$ and hydrostatic stress $\sigma(x,t)$ are two coupled variables to be solved. Based on the modified Eshelby's solution (Appendix A), we obtained the following equations,

$$\sigma_x = -\frac{E_c(1+v_c+\varphi+\varphi v_m)}{3[(1+v_c)(1-2v_c)+\varphi(1+v_m)]L}\int_0^L\int_{C_{a0}}^{C_a}(1-f)\frac{dC_a}{C_a}dx \tag{29}$$

$$\sigma_y = \sigma_z = -\frac{1}{(1-v_c+\varphi+\varphi v_m)}\left(\frac{E_c}{3}\int_{C_{a0}}^{C_a}(1-f)\frac{dC_a}{C_a}+\sigma_x v_c\right) \tag{30}$$

$$\theta = \frac{1}{3(1-v_c+\varphi+\varphi v_m)}\left[(1+v_c+3\varphi+3\varphi v_m)\int_{C_{a0}}^{C_a}(1-f)\frac{dC_a}{C_a}-\frac{(1+v_c+\varphi+\varphi v_m)^2(1-2v_c)}{[(1+v_c)(1-2v_c)+\varphi(1+v_m)]L}\int_0^L\int_{C_{a0}}^{C_a}(1-f)\frac{dC_a}{C_a}dx\right] \tag{31}$$

where E_c and v_c are the Young's modulus and Poisson's ratio of Al, respectively. E_m and v_m are the Young's modulus and Poisson's ratio of passivation material, respectivey. φ is the ratio of E_c to E_m (φ=E_c/E_m). Applying the above equations to Eq. (19), the governing equations for atomic concentration and hydrostatic stress were obtained as follows:

$$\frac{1+v_c+3(1+v_m)\varphi}{3(1-v_c+\varphi+\varphi v_m)}\frac{1-f}{C_a}\frac{\partial C_a}{\partial t}-\frac{(1+v_c+\varphi+\varphi v_m)^2(1-2v_c)}{3[(1+v_c)(1-2v_c)+\varphi(1+v_m)](1-v_c+\varphi+\varphi v_m)L}\int_0^L\frac{1-f}{C_a}\frac{\partial C_a}{\partial t}$$

$$= D_a\left[-\frac{Z^*e\rho j}{k_BT}\frac{\partial C_a}{\partial x}+\frac{\partial^2 C_a}{\partial x^2}+\frac{2E_c\Omega}{9(1-v_c+\varphi+\varphi v_m)k_BT}\left[(1-f)\frac{\partial^2 C_a}{\partial x^2}-\frac{\partial f}{\partial C_a}\left(\frac{\partial C_a}{\partial x}\right)^2\right]\right] \tag{32}$$

$$\sigma = -\frac{2E_c}{9(1-v_c+\varphi+\varphi v_m)}\left[\int_{C_{a0}}^{C_a}\frac{1-f(C_a)}{C_a}dC_a+\frac{(1+v_c+\varphi+\varphi v_m)^2\int_0^L\int_{C_{a0}}^{C_a}\frac{1-f(C_a)}{C_a}dC_a dx}{2[(1+v_c)(1-2v_c)+\varphi(1+v_m)]L}\right] \tag{33}$$

For a Blech structure, above equations were solved numerically with the initial condition (Eq. (23)) and the following boundary conditions,

$$J_a(0,t) = \frac{Z^*e\rho j}{k_BT}C_a(0,t)-\left[1+\frac{2E_c(1-f)}{9[1-v_c+\varphi+\varphi v_m]}\frac{\Omega}{k_BT}\right]\frac{\partial C_a(0,t)}{\partial x}=0 \tag{34}$$

$$J_a(L,t) = \frac{Z^*e\rho j}{k_BT}C_a(L,t)-\left[1+\frac{2E_c(1-f)}{9[1-v_c+\varphi+\varphi v_m]}\frac{\Omega}{k_BT}\right]\frac{\partial C_a(L,t)}{\partial x}=0 \tag{35}$$

For a SWEAT structure, with the boundary conditions of Eq. (22), The solution of Eq. (32) is a constant atomic concentration for the entire metal line at all the times, and the hydrostatic stress is a constant as follows,

$$C_a(x,t) = C_{a0} \tag{36}$$

$$\sigma(x,t) = \text{constant} \tag{37}$$

3.3. Failure criterion and steady-state solutions

For both un-passivated and passivated configurations, when the atomic concentration $C_a(x,t)$ decreases to its critical value $C_{a,critical}$, the failure takes place due to void formation as follows.

$$C_a(x,t) = C_{a,critical} \tag{38}$$

where $C_{a,critical}$ is a material property. The time to failure, $t_{failure}$, can then be determined using the numerical results of Eq. (24) or (32) for the un-passivated or passivated configurations, respectively.

To determine $C_{a,critical}$, the steady-state equation of the un-passivated configuration, where the term on the left side of Eq. (24) became zero, was

$$-\frac{Z^*e\rho j}{k_BT}\frac{\partial C_a}{\partial x}+\frac{\partial^2 C_a}{\partial x^2}=0 \tag{39}$$

Solving this equation, and assuming that void and hillock form at the same time, we had

$$\frac{C_{\mathrm{a,critical}}}{C_{a0}} = 2\left[\exp\left[\frac{Z^* e\rho (jL)_c}{2k_B T}\right] + 1\right]^{-1} \tag{40}$$

where L_c is the critical length under the given current density, which can be obtained from experiment, thereby $C_{\mathrm{a,critical}}$ can be determined by Eq. (40).

Knowing $C_{\mathrm{a,critical}}$, the threshold product $(jL)_c$ in terms of the critical atomic concentration can be obtained as follows:

$$(jL)_c\big|_{\mathrm{un-passivated}} = \frac{k_B T}{Z^* e\rho}\ln\left(\frac{2C_{\mathrm{a0}}}{C_{\mathrm{a,critcial}}} - 1\right) \tag{41}$$

Similarly, at the steady state, Eq. (32) for the passivated configuration became,

$$-\frac{Z^* e\rho j}{k_B T}\frac{\partial C_a}{\partial x} + \frac{\partial^2 C_a}{\partial x^2} + \frac{2E_c\Omega}{9(1-\nu_c+\varphi+\varphi\nu_m)k_B T}\left[(1-f)\frac{\partial^2 C_a}{\partial x^2} - \frac{\partial f}{\partial C_a}\left(\frac{\partial C_a}{\partial x}\right)^2\right] = 0 \tag{42}$$

and the threshold product $(jL)_c$ was obtained as follows,

$$(jL)_c\big|_{\mathrm{passivated}} = \frac{k_B T}{Z^* e\rho}\left[1 + \frac{2E_c(1-f)\Omega}{9[1-\nu_c+(1+\nu_m)\varphi]k_B T}\right]\ln\left(\frac{2C_{\mathrm{a0}}}{C_{\mathrm{a,critcial}}} - 1\right) \tag{43}$$

Details to obtain the steady-state solutions were given in Appendix B.

3.4. Void growth model

When voids were formed, the following equation for the drift velocity of void growth was obtained at x=0

$$V_{\mathrm{drift}} = \Omega L\left.\frac{dJ_a}{dx}\right|_{x=0} \tag{44}$$

where

$$\left.\frac{dJ_a}{dx}\right|_{x=0} = D_a\left(\left.\frac{Z^* e\rho j}{k_B T}\frac{\partial C_a}{\partial x}\right|_{\substack{x=0\\ t=t(failure)}} - \left.\frac{\partial^2 C_a}{\partial x^2}\right|_{\substack{x=0\\ t=t(failure)}}\right) \tag{45}$$

In the un-passivated configuration. The diffusivity D_a can then be determined as follows

$$D_a = V_{\mathrm{drift}}\Omega^{-1}L^{-1}\left[\left.\frac{Z^* e\rho j}{k_B T}\frac{\partial C_a}{\partial x}\right|_{\substack{x=0\\ t=t(\mathrm{failure})}} - \left.\frac{\partial^2 C_a}{\partial x^2}\right|_{\substack{x=0\\ t=t(\mathrm{failure})}}\right]^{-1} \tag{46}$$

where V_{drift} can be measured from the experiment. The void length in the un-passivated metal line can be calculated after knowing Da, as follows.

$$L_{\mathrm{void}}\big|_{\mathrm{un-passivated}} = \Delta t V_{\mathrm{drift}} = \Delta t\Omega L D_a\left[\left.\frac{Z^* e\rho j}{k_B T}\frac{\partial C_a}{\partial x}\right|_{\substack{x=0\\ t=t(\mathrm{failure})}} - \left.\frac{\partial^2 C_a}{\partial x^2}\right|_{\substack{x=0\\ t=t(\mathrm{failure})}}\right] \tag{47}$$

where Δt is the total testing time minus time of void formation, $\Delta t = t_{\mathrm{total}} - t_{\mathrm{failure}}$.

In the elastically-passivated configuration, in a similar approach, we can obtain the void length as follows,

$$L_{\mathrm{void}}\big|_{\mathrm{passivated}} = \Delta t\Omega L D_a\left[-\left.\frac{Z^* e\rho j}{k_B T}\frac{\partial C_a}{\partial x}\right|_{\substack{x=0\\ t=t(\mathrm{failure})}} + \frac{\partial^2 C_a}{\partial x^2} + \frac{2E_c\Omega}{9(1-\nu_c+\varphi+\varphi\nu_m)k_B T}\left[(1-f)\left.\frac{\partial^2 C_a}{\partial x^2}\right|_{\substack{x=0\\ t=t(\mathrm{failure})}} - \frac{\partial f}{\partial C_a}\left(\left.\frac{\partial C_a}{\partial x}\right|_{\substack{x=0\\ t=t(\mathrm{failure})}}\right)^2\right]\right] \tag{48}$$

4. Results and discussion

According to the experimental results in Section 2, the critical length L_c was 10 μm and 15 μm for Al without and with annealing, respectively, under a current density of 1 MA/cm^2. Therefore, $C_{\mathrm{a,critical}}$ was determined based on Eq. (40). Subsequently, the atomic diffusivity D_a was determined based on Eq. (46), using the experimental data of the drift velocity for the 100 μm-length and 200 nm-

Table 1
Critical atomic concentration $C_{a,crictial}$ and atomic diffusivity D_a determined based on Eqs. (40) and (46).

Property	without annealing	with annealing
$C_{a,critical}$	$0.965C_{a0}$	$0.949C_{a0}$
D_a	8.5×10^{-15} m^2/s	4.8×10^{-15} m^2/s

Table 2
Material properties of Al and Si_3N_4 (passivation).

Property	Value
Atomic volume (Ω)	1.66×10^{-29} m^3
Electrical resistivity (ρ)	3.22×10^{-8} Ohm•m
Electric charge (e)	1.6×10^{-19} C
Charge number (Z^*)	1.1 [19]
Young's modulus (E_m)	60 GPa
Poisson's ratio of Al (ν_m)	0.33
Young's modulus of Si_3N_4 (E_c)	100 GPa
Poisson's ratio of Si_3N_4 (ν_c)	0.23
Vacancy volume relaxation factor (f)	Eq. (15)

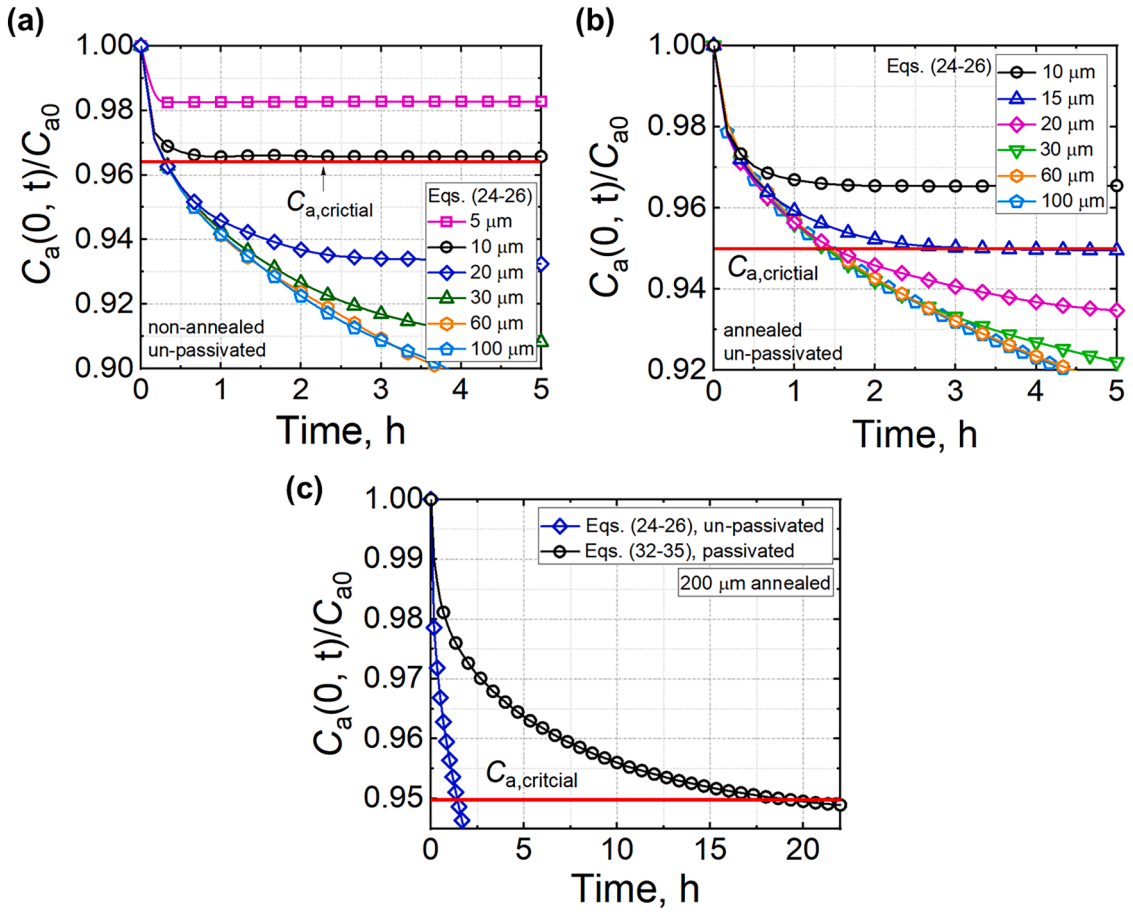

Fig. 10. Numerical results for the evolution of the normalized atomic concentration C_a/C_{a0} in Al specimens with Blech structure under the current density of 1 MA/cm^2. (a) C_a/C_{a0} at the cathode side ($x = 0$) over time for 5/10/20/30/60/100 μm conductors without annealing and without passivation. (b) C_a/C_{a0} at the cathode side ($x = 0$) over time for 10/15/20/30/60/100 μm conductors without passivation but with annealing. (c) Comparison of C_a/C_{a0} at cathode side over time in un-passivated and passivated 100 μm conductor after annealing.

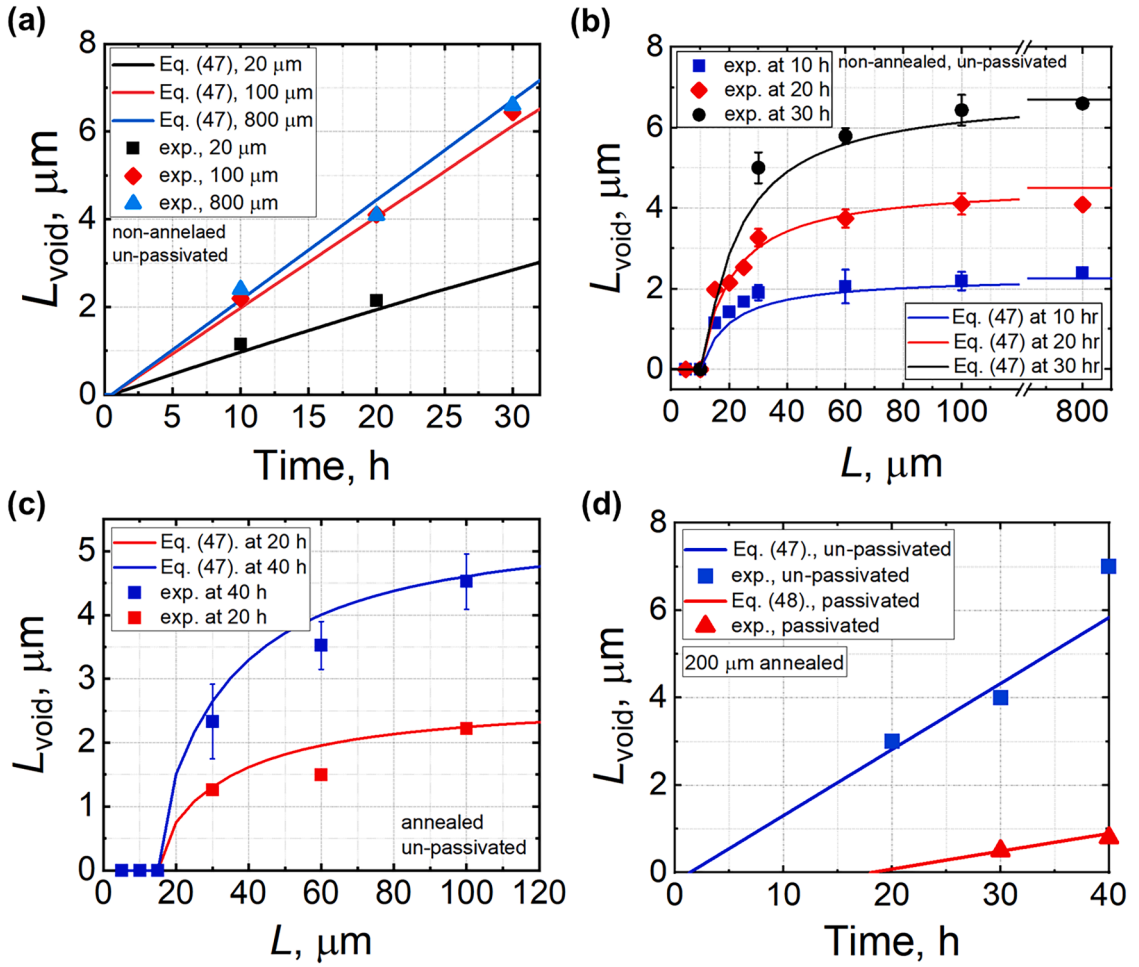

Fig. 11. Predictions of void growth with Blech structure under the current density of 1 MA/cm^2 in comparison with experimental data. (a) Void growth in 20/100/800 μm bare conductors without annealing from 0 to 35 h. (b) Void growth in the conductors (without annealing) with varying lengths from 0 to 800 μm at 10/20/30 h. (c) Void length in annealed conductors in varying lengths at 20/40 h. (d) Void growth in 200 μm passivated and un-passivated conductors (after annealing) from 0 to 40 h.

thick specimens, $V_{drift} = 0.0608 \pm 0.005$ nm/s and 0.0313 ± 0.003 nm/s for Al without and with annealing, respectively. Table 1 summarizes the obtained material properties $C_{a,crictial,}$ and D_a. Other material properties used in Eqs. (40) and (46) were given in Table 2. The detailed procedures to determine $C_{a,crictail}$ and D_a were given in Appendix C.

In the following, we first used the physical and material properties in Table 1 and Table 2 to predict the time to failure and void growth in various experiments. After verifying the simulation results with the experimental data, we discussed the critical atomic concentration. Furthermore, we theoretically determined the critical threshold products of current density and conductor length for un-passivated and passivated configurations. Finally, we simulated the exponent of current density n based on our models.

4.1. *Experimental verification*

First, the time to failure was calculated based on Eqs. (24-26) and (32-35) for each testing condition in the experiments described in Section II. Fig. 10 plotted the predicted evolution of the normalized atomic concentration C_a/C_{a0} at the cathode side ($x = 0$) in various situations. The solid horizontal lines in red color in the figures represented the normalized critical atomic concentration $C_{a,\ critical}/C_{a0}$. In Fig. 10(a)) for Al without annealing, $C_a/\ C_{a0}$ for the lengths of 5 and 10 μm always stayed above $C_{a,\ critical}/C_{a0}$ after the steady state, indicating no EM failure. EM failure would occur approximately at 20 min for the conductor length 20 μm or greater, almost at the same time. We observed EM failures at 30 min with lengths of 30/60/100 μm in the experiment. Fig. 10(b) showed that the EM failure would occur at 1.5 h for a length of 20 μm or greater after annealing. Moreover, Fig. 10(c) further predicted EM failure after 15 h for passivated configuration with annealing. These results were consistent with the experimental data.

Fig. 11 displayed the numerical results for void growth under various situations. Fig. 11(a) and (b) showed the predicted void length versus time and conductor length, respectively, for Al without annealing. Void length almost linearly increased over time and

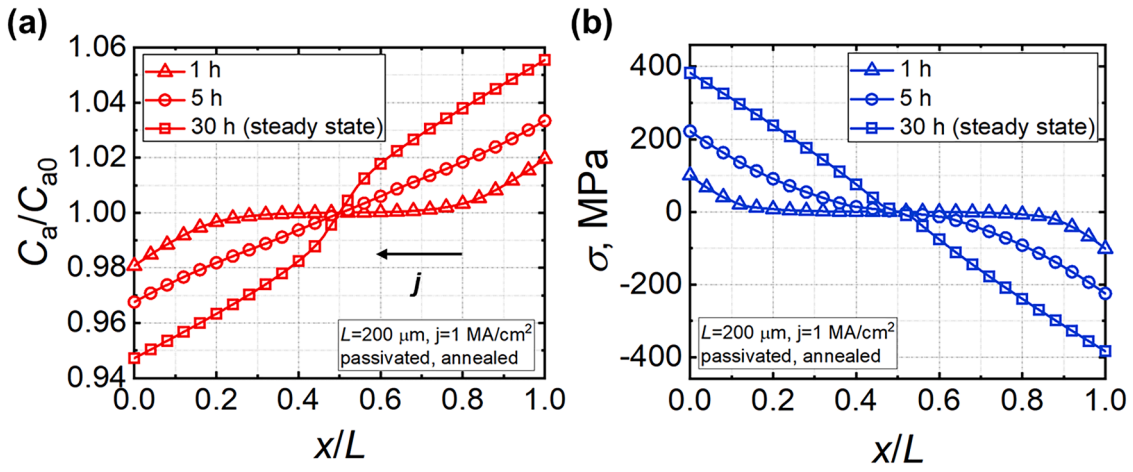

Fig. 12. (a) Simulation results for the atomic concentration along 200 μm passivated Al line under a current density of 1 MA/cm^2 at various times. (b) Simulation results for the hydrostatic stress along 200 μm passivated Al line under a current density of 1 MA/cm^2 at various times.

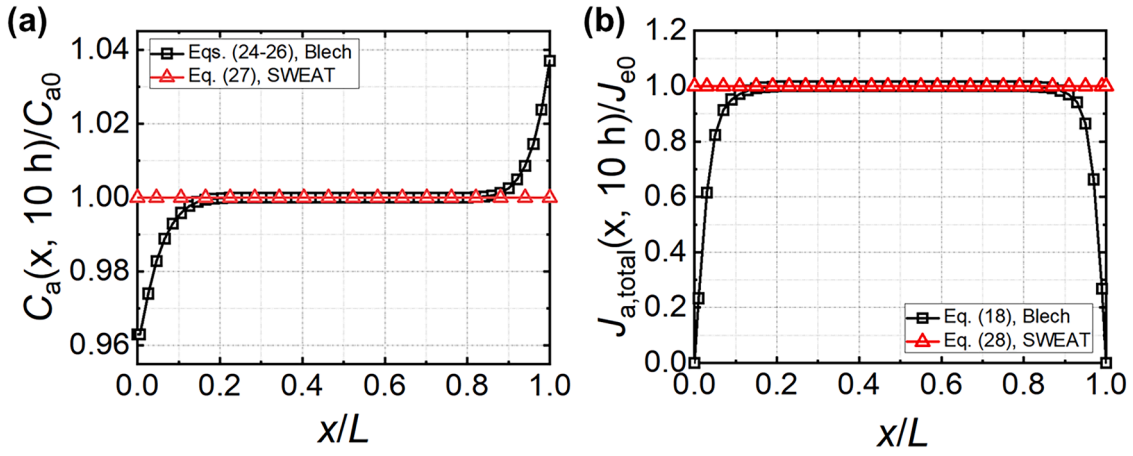

Fig. 13. Comparison of atomic concentration and flux distributions at 10 h between Blech and SWEAT structures under the current density of 1 MA/cm^2. (a) Distribution of atomic concentration in 800 μm-length Blech and SWEAT structures. (b) Distribution of atomic fluxes in 800 μm-length Blech and SWEAT structures. Here the total atomic fluxes in Blech and SWEAT structures were obtained using Eqs. (18) and (28), respectively. J_{e0} was the initial atomic flux due to electron wind, $J_{e0} = (D_a C_{a0}/k_B T)Z^* e\rho j$.

grew more rapidly in the longer conductor. However, the void size in the 800 μm sample was just slightly larger than that in the 100 μm length. For the conductor's length greater than 60 μm, the void growth leveled off against the conductor length. A similar trend was also found for Al with annealing, as shown in Fig. 11(c). Moreover, for the annealed conductor, Fig. 11(d) showed that void growth in passivated conductors was significantly slower than that in un-passivated conductors. These simulation results agreed well with the experimental data.

Figs. 10 and 11 have important implications on the effect of self-diffusion and mechanical stress on EM failure. When mechanical stress is absent, such as in the un-passivated configuration, the atomic concentration gradient is the only resistive force against electron wind force. Therefore, self-diffusion plays a dominant role in EM development. Shatzkes and Lloyd (Shatzkes and Lloyd, 1986) also derived a 1-D solution without considering the effect of the stress gradient, but their results indicated the steady state was reached in milliseconds. Our current model is consistent with the experimental results, as shown in Figs. 10(a) and 11(a), (b). When mechanical stress is present, such as in passivated configuration, mechanical stress gradient made a significant impact on the EM development, as the time to failure, based on Fig. 10(c), was about 10 times longer than that without mechanical stress.

To further understand atomic transport behavior and stress development during EM, Fig. 12(a) plotted the simulation results of atomic concentration for the passivated Al with a length of 200 μm at different time intervals. C_a decreased at the cathode side, indicating void formation and growth, and increased at the anode side for hillock build-up. Correspondingly, Fig. 12(b) showed the tensile hydrostatic stress σ generated at the cathode side due to the depletion of atoms and the compressive hydrostatic stress at the anode due to the accumulation of atoms. At the steady state, the maximum σ reached about 400 MPa. This result was consistent with the results reported in the literature.

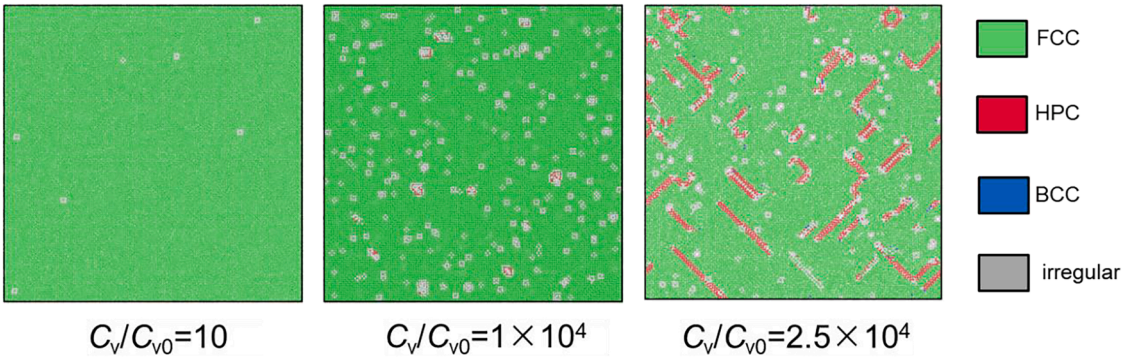

Fig. 14. Lattice structure of Al without mechanical constrain at different vacancy concentrations.

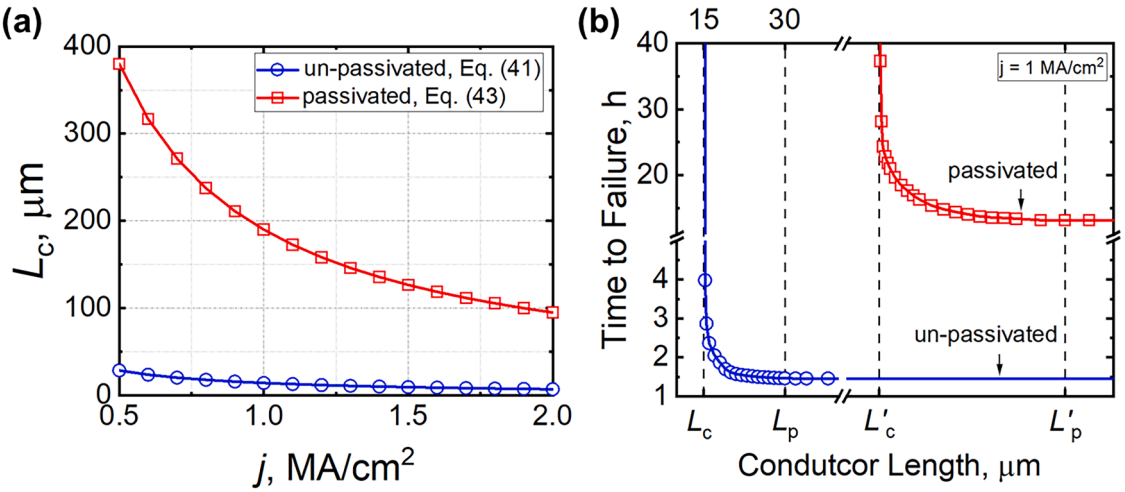

Fig. 15. (a) Predicted threshold products $jL = (jL)_c$ curves in the un-passivated and passivated Al using Eqs. (41) and (43). (b) Time to failure versus conductor length using Eqs. (41) and (43) in un-passivated and passivated Al under the current density of 1 MA/cm^2.

For the comparison between Blech and SWEAT structures, Fig. 13 plotted the results of the distribution of C_a/C_{a0} and the flux $J_{a,total}/J_{a,e0}$ at 10 h. For the Blech structure, C_a decreased at the cathode and increased at the anode, indicating the void formation at the cathode and hillock formation at the anode. For the SWEAT structure, however, C_a remained constant for the entire length, indicating no EM damage. Fig. 13(b) showed that the atomic flux in a majority length of the Blech structure remained constant except for the rapid change at the two ends. But in the SWEAT structure, a constant flow of atomic flux occurred over the entire conductor, showing continuous atomic transport. With the temperature gradient neglected under the current density of 1 MA/cm^2, the theoretical results were consistent with the experimental observations. For the EM in SWEAT structures under elevated temperatures, extensive theoretical results with and without considering temperature gradients were presented and discussed in the second part of this work (Cui et al., 2023).

4.2. $C_{a,critical}$

Critical atomic concentration, $C_{a,critical}$, is an important material's property to determine the void initiation during EM. Such a property has not been determined previously. As discussed in the introduction, the predicted vacancy concentration was only in the range of 2 - 4C_{v0} at failure, according to most of the models (Clement, 1997; Cui et al., 2019; Shatzkes and Lloyd, 1986; Sukharev et al., 2007) in literature. Based on the values shown in Table 1, the corresponding critical vacancy concentration $C_{v,critical}$ in our study was 4 × 10$^4C_{v0}$, which implied that 40,000 vacancies were generated per one million atoms at the failure site. To further understand the meaning of this value, MD simulations were performed to investigate the microstructure in Al at different vacancy concentrations. Fig. 14 plotted the lattice structure of Al at various vacancy concentrations, in which the green region represents FCC lattice structure, the red region is the HPC lattice structure, and the blue region is the BCC lattice structure. At the low vacancy concentration level, e.g., at 10C_{v0}, the system was FCC-dominated, which means that the vacancies in Al are isolated from each other. However, with the increasing vacancy concentration, the exchanging position between atoms and vacancies would promote the accumulation of vacancies. Thus, the HPC lattice structure clusters appear randomly. When the vacancy concentration was increased to 10$^4C_{v0}$, there

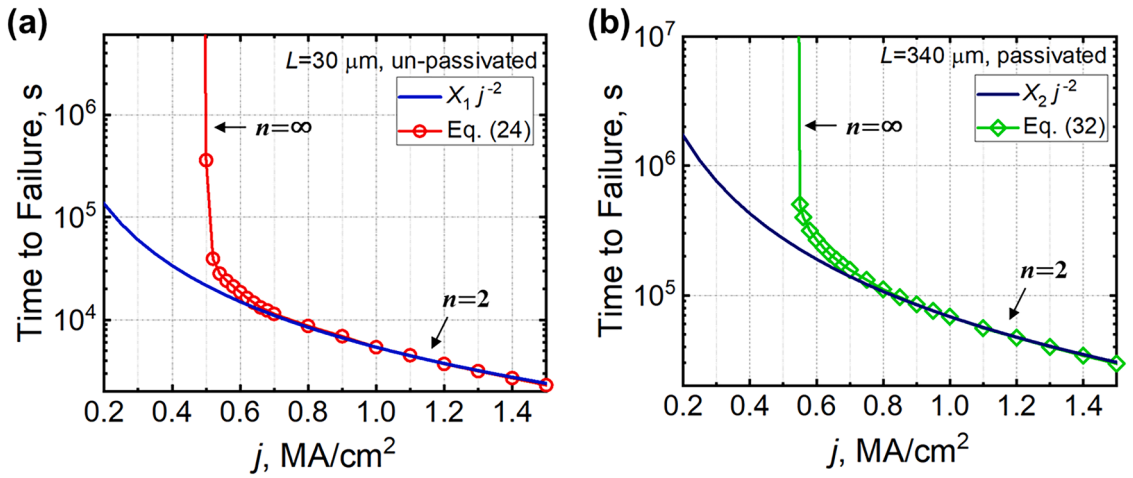

Fig. 16. Predictions of the current density exponent n for time to failure. (a) un-passivated Al line, and X_1=5.4 × 10^{23} A•s/m^2; (b) passivated Al line, and X_2=6.84 × 10^{24} A•s/m^2.

were some tiny voids observed. With further increased vacancy concentration, massive dislocations are generated, indicating voids forming. Therefore, we confirmed the plausibility of the critical atomic concentrations shown in Table 1 through MD simulation.

4.3. $(jL)_c$ and L_p

Blech developed a concept of the critical threshold product of current density and conductor length, below which the conductor is immune from EM failure (Blech, 1976). The threshold product was expressed as follows,

$$jL = (jL)_c \tag{49}$$

where the critical threshold product $(jL)_c$ was experimentally determined in Blech's study (Blech, 1976). Blech's theory has several implications. First, the critical threshold product could not be determined according to Blech's theory, but experimentally for each testing condition. Second, the critical hydrostatic stress or its gradient was not a unique constant because different critical threshold products were obtained for Al in un-passivated and passivated configurations. Additionally, numerous studies showed that EM developed more rapidly in an un-passivated configuration, where mechanical stress was not present or at a much lower level. Blech's theory could conclude that no EM damage would occur in the un-passivated configuration.

In this work, the threshold product $(jL)_c$ was determined theoretically using Eqs. (41) and (43) after knowing $C_{a,critical}$. Fig. 15(a) plotted the curves of threshold product for un-passivated and passivated configurations accordingly, in which two critical products are based on a single $C_{a,critical}$. Clearly, it showed that under passivated configuration, the conductor allowed a much greater current density with the same length compared to the un-passivated configuration. This prediction agreed with present experimental observations.

Furthermore, after the threshold product exceeds the critical value, EM failure takes place during the transient state, as seen in Fig. 10. Therefore, the transient solutions using Eqs. (24-26) and (32-35) are needed. Fig. 15(b) plotted the time to failure versus conductor length under the current density of 1 MA/cm^2. Three regions were identified from this figure: when $L < L_c$, no EM failure and thereby the steady-state solution was valid. When $L_c < L < L_p$, the time to failure decreased with increasing length. When $L > L_p$, the time appeared independent of the conductor length. Therefore, in addition to the critical length L_c defined by Blech, there existed another important length L_p, beyond which the failure time remains unchanged. L_p was approximately twice the critical length according to the simulation results in Fig. 15 (b).

It is worth noting that the threshold product applies to Blech structures only when the conductor is in perfectly blocking conditions at both ends. Design rules based on the threshold product do not exist in the SWEAT structure, as we showed that no EM damage would occur under the given current density in the SWEAT structures.

4.4. Current density exponent n

The study conducted by Black *et al.* (Black, 1969) showed that the inverse of the mean time to failure of a conductor line under EM was proportional to the square of the current density, as follows,

$$\frac{1}{\mathrm{MTF}} = Xj^n \tag{50}$$

where MTF is the mean time to failure, X is a constant that contains the physical properties of the interconnect, and $n = 2$. This equation

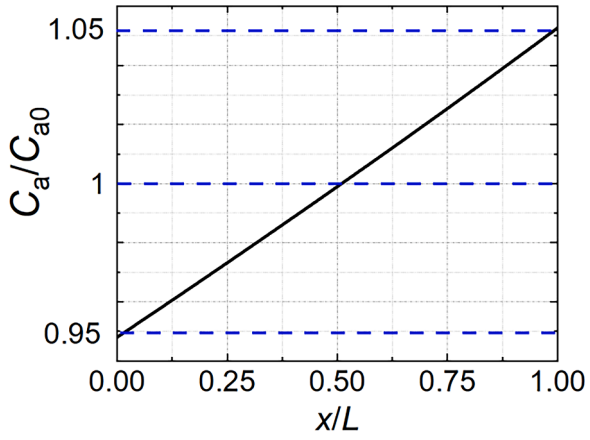

Fig. B. Simulation results for the distribution of normalized atomic concentration at steady state for 15 μm Al without passivation.

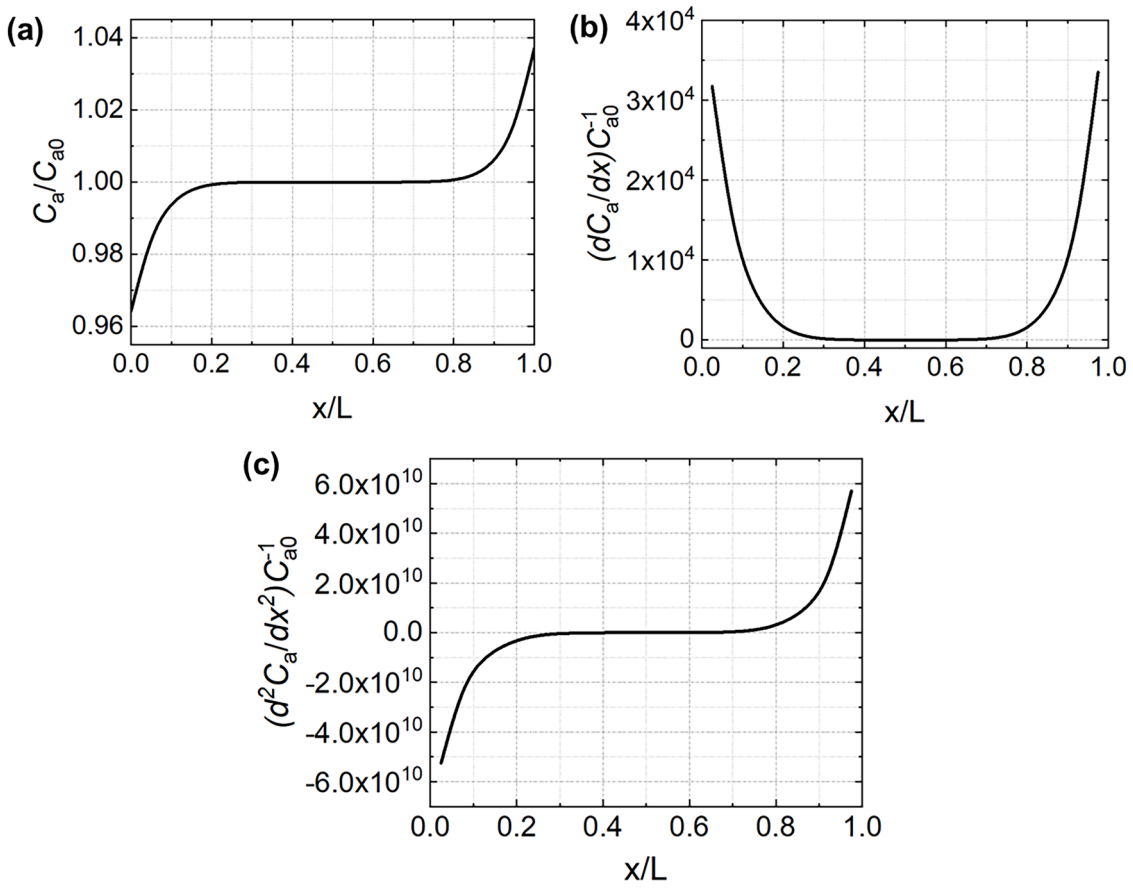

Fig. C. The numerical results for the distributions of C_a/C_{a0}, $(dCa/dx)/C_{a0}$, and $(d^2Ca/dx^2)/C_{a0}$ in 100 μm Al without annealing at the moment for C_a reaching $C_{a,critical}$ $(0.965C_{a0})$.

was derived from a simple theory by (Black, 1967). Since then, several EM studies have been conducted to verify the value of the current density exponent n. In literature, the reported n-value varies greatly as follows: $1 \leq n \leq 2$ (Børgesen et al., 1992a; Gambino et al., 2009; Hu et al., 1999; Zhang et al., 2013), $n = 4$ (Hemmert and Costa, 1991; Tezaki et al., 1990), $n = 4.5$ (Kraft and Arzt, 1998), $n = 4.9$ (Gardner et al., 1987; Yuzuriha and Early, 1986), $n = 5$ (Børgesen et al., 1992b), or n as high as 10 (Ho and Kwok, 1989). It should be noted that the value of current density exponent n during practical conditions could be different from what was applicable during accelerated tests.

In this study, Eqs. (24-26) and (32-35) were applied to study the current density exponent n. Fig. 16 plotted the time to failure against the current density in a range of 0.2 – 1.4 MA/cm^2, using Eqs. (24) and (32), respectively, for the un-passivated and passivated configurations. As an illustration, the conductor length was chosen as $L = L_p = 30$ μm in the un-passivated configuration and $L = L_p = 340$ μm in the passivated configuration. The curve with exponent $n = 2$ using Eq. (50) was also plotted in those figures. When the current ranged from 0.8 – 1.4 MA/cm^2, the exponent followed approximately as $n = 2$. However, when the current density decreased further, the failure time did not follow the $n = 2$ anymore because the threshold product fell below the critical value, the failure time approaching infinity. This implies that if the current density in use conditions is substantially lower than the current density in the accelerated test, $n = 2$ is not valid anymore. For the accelerated test in EM, depending on the range of the current density, the exponent can be very different. In a certain range of current density, the exponent maintains a value of 2, and then it rapidly increases and approaches infinity if the current density falls below the critical current density. It must be noted that the above discussions are applied to the Blech structure-like only. For SWEAT-like structures, no EM damage would be expected with the given current density.

5. Conclusion

We presented a comprehensive and integrated study of EM driven by interacting electrical, diffusive, thermal, and mechanical fields through experiment, theory, and numerical simulation. First, both Blech and SWEAT structures of various lengths, using aluminum (Al) conductor as a carrier, were designed and fabricated on silicon wafers, which were annealed and/or passivated as needed. Extensive experimental tests were performed to record the progression of EM under various conditions. Second, we introduced a coupled EM theory, in which a molecular dynamics (MD)-based diffusion-induced strain equation was incorporated. Third, theoretical and experimental methods for determining the critical atomic concentration were established. Moreover, a void growth model for Blech structure was developed to determine the material's diffusivity. These physical properties were then applied to various situations, and the results were verified experimentally. The main conclusions of this study are summarized below.

1 The critical atomic concentration of aluminum was determined as $C_{a,critical} = 0.965C_{ao}$ and $0.949C_{ao}$ (C_{ao} is the initial atomic concentration), before and after annealing, respectively. Such values corresponded to a critical vacancy concentration in the range of $10^4 \sim 10^5 C_{v0}$ (C_{v0} is the initial vacancy concentration). We further confirmed the plausibility of $C_{a,critical}$ through MD simulation.
2 We derived 1D analytical solutions for un-passivated and passivated configurations, respectively. The modified Eshelby's solution was used for obtaining an approximate analytical solution in an elastically passivated configuration. The predicted time to failure and void growth under various conditions agreed well with experimental results. In the absence of mechanical stress under un-passivated configurations, atomic concentration gradient became the only balancing force against electron wind force in EM development. However, when mechanical stress was present, such as in passivated configurations, stress migration played an important role in resisting EM development, increasing the failure time by a factor of about 10. The predicted maximum hydrostatic stress was about 400 MPa, which is consistent with the results in the literature.
3 Under the current density of 1 MA/cm^2, the SWEAT structure did not have any damage but a constant atomic flux across the entire conductor. Therefore, the effects of joule heating and temperature gradient could be neglected.
4 The critical threshold products of current density and conductor length were determined for un-passivated and passivated configurations, respectively, after knowing $C_{a,critical}$. The original Blech's theory cannot determine the critical threshold product without additional testing data in each configuration. And Blech's theory, which considered stress gradient only, failed to explain a more rapid EM development in un-passivated configurations.
5 We discovered another important conductor length L_p, beyond which the time to failure due to EM is independent of the conductor's length. L_p is approximately twice the critical length L_c.
6 We investigated the current density exponent n based on our models for un-passivated and passivated configurations. In a certain range of current density, the failure time due to EM follows Black's law with the exponent of 2. However, Black's law provides a much more conservative estimate in a low level of current density in practical conditions.
7 EM design rules, either based on the threshold product concept or current exponent n, do not exist in the SWEAT-like interconnect structures, as no EM damage will occur under given the current density in SWEAT structures.

This paper selected Al as a carrier for EM study, but the theory and experimental methods can now be extended to other interconnect material systems in micro-/nano-electronics. EM can be interstitial (Chao et al., 2006), substitutional (Ho and Kwok, 1989), or along the surface (Kraatz et al., 2016). We can also extend the theory and experiment to investigate surface EM or interstitial EM. It is noted that, in this study, we reported the results under the current density of 1 MA/cm^2 only, in which we neglected the effect of the joule heating and temperature gradient. The study of EM considering thermomigration was reported separately (Cui et al., 2023) in the second part of this work.

CRediT authorship contribution statement

Zhen Cui: Methodology, Software, Investigation, Formal analysis, Validation, Visualization, Writing – original draft. **Xuejun Fan:** Conceptualization, Methodology, Investigation, Formal analysis, Supervision, Validation, Visualization, Writing – original draft. **Yaqian Zhang:** Methodology, Investigation. **Sten Vollebregt:** Methodology, Validation, Supervision, Writing – review & editing. **Jiajie Fan:** Writing – review & editing. **Guoqi Zhang:** Supervision, Resources, Writing – review & editing.

Declaration of Competing Interest

The authors declare that they have no known competing financial interest or personal relationships that could have appeared to influence the work reported in this paper.

Data availability

Data will be made available on request.

Acknowledgements

The authors would like to thank the staff of the Else Kooi Laboratory for processing support. Xuejun Fan would like to acknowledge the support from Lamar University and Delft University of Technology (TU Delft) during his sabbatical leave at TU Delft. He also would like to acknowledge his former doctoral student, Dr. Kasemsak Kijkanjanapaiboon, for his dedication and diligence during his doctoral study of this topic.

Appendix A. Modified Eshelby's solution

To obtain an approximate solution for passivated metal line, the metal line was idealized as a cylindrical shape, as shown in Fig. 9. The metal line was laterally passivated by elastic material, and both ends of conductor were constrained. When the conductor has an eigenvalue ε_{ij}^{*} as follows,

$$\varepsilon_{ij}^{*} = \varepsilon^{*}\delta_{ij} \tag{A.1}$$

where ε^{*} can be diffusion-induced strain or thermal strain. Based on Hooke's law, the stress-strain relationship with eigenvalue can be written as follows,

$$\sigma_x = 2G(\varepsilon_x - \varepsilon^{*}) + \lambda(\varepsilon_{kk} - 3\varepsilon^{*}) \tag{A.2}$$

$$\sigma_y = 2G(\varepsilon_y - \varepsilon^{*}) + \lambda(\varepsilon_{kk} - 3\varepsilon^{*}) \tag{A.3}$$

$$\sigma_z = 2G(\varepsilon_z - \varepsilon^{*}) + \lambda(\varepsilon_{kk} - 3\varepsilon^{*}) \tag{A.4}$$

where ε_x, ε_y, and ε_z are total strains in x, y, and z directions, respectively. And, $\varepsilon_{kk} = \varepsilon_x + \varepsilon_y + \varepsilon_z$. σ_x, σ_y, and σ_z are mechanical stresses in x, y, and z directions, respectively. G and λ are Lame's constants, $G = \frac{E_c}{2(1+\nu_c)}$ and $\lambda = \frac{E_c\nu_c}{(1+\nu_c)(1-2\nu_c)}$. E_c and ν_c are the Young's modulus and Poisson's ratio of conductor, respectively. Then, above equation can be equivalently rewritten as follows,

$$0 = 2G\left[\varepsilon_x - \left(\varepsilon^{*} + \frac{\sigma_x}{E_c}\right)\right] + \lambda\left[\varepsilon_{kk} - \left(3\varepsilon^{*} + \frac{\sigma_x}{E_c} - \frac{2\nu_c\sigma_x}{E_c}\right)\right] \tag{A.5}$$

$$\sigma_y = 2G\left[\varepsilon_y - \left(\varepsilon^{*} - \frac{\nu_c\sigma_x}{E_c}\right)\right] + \lambda\left[\varepsilon_{kk} - \left(3\varepsilon^{*} + \frac{\sigma_x}{E_c} - \frac{2\nu_c\sigma_x}{E_c}\right)\right] \tag{A.6}$$

$$\sigma_z = 2G\left[\varepsilon_z - \left(\varepsilon^{*} - \frac{\nu_c\sigma_x}{E_c}\right)\right] + \lambda\left[\varepsilon_{kk} - \left(3\varepsilon^{*} + \frac{\sigma_x}{E_c} - \frac{2\nu_c\sigma_x}{E_c}\right)\right] \tag{A.7}$$

Eqs. (A.5) -(A.7) can be considered as a plane stress problem with the new eigenvalue $\varepsilon_{ij}^{'}$,

$$\varepsilon^{'}{}_x = \varepsilon^{*} + \frac{\sigma_x}{E_c} \tag{A.8}$$

$$\varepsilon^{'}{}_y = \varepsilon^{'}{}_z = \varepsilon^{*} - \frac{\nu_c\sigma_x}{E_c} \tag{A.9}$$

To obtain a complete stress-strain relation, we still need a relation between $\varepsilon_{ii}^{'}$ and ε_{ii}. Based on the Eshelby's theory, this relation can be expressed as follows,

$$\varepsilon_{ij} = S^{'}{}_{ijkl}\varepsilon^{'}{}_{kl} \tag{A.10}$$

where the plane-stress inhomogeneity Eshelby's tensor ($S^{'}{}_{ijkl}$) is,

$$S'_{ijkl} = \begin{bmatrix} 1 & A+\frac{v_m}{2}(B+C) & A+\frac{v_m}{2}(B+C) \\ 0 & \frac{5+v_m}{8}B+\frac{3v_m-1}{8}C & \frac{5+v_m}{8}C+\frac{3v_m-1}{8}B \\ 0 & \frac{5+v_m}{8}C+\frac{3v_m-1}{8}B & \frac{5+v_m}{8}B+\frac{3v_m-1}{8}C \end{bmatrix}$$

and:

$$A = -\frac{E_c v_m - E_m v_c}{E_c + E_m + E_c v_m - E_m v_c}$$

$$B = \frac{E_c(5E_c + 3E_m + E_c v_m - E_m v_c)}{-E_c^2 v_m^2 + 2E_c^2 v_m + 3E_c^2 + 2E_c E_m v_c v_m - 2E_c E_m v_c + 4E_c E_m - E_m^2 v_c^2 + E_m^2}$$

$$C = \frac{E_c(E_c - E_m - 3E_c v_m + 3E_m v_c)}{-E_c^2 v_m^2 + 2E_c^2 v_m + 3E_c^2 + 2E_c E_m v_c v_m - 2E_c E_m v_c + 4E_c E_m - E_m^2 v_c^2 + E_m^2}$$

where E_m and ν_m are the Young's modulus and Poisson's ratio for passivation material, respectively

Applying the Eqs. (A.8) and (A.9) to Eq. (A.10), we can obtain the ε_{ij} as follows,

$$\varepsilon_x = \frac{(1+v_c)(1-2v_c)+\varphi(1+v_m)}{E_c(1+\varphi-v_c+\varphi v_m)}\sigma_x + \frac{1+\varphi+\varphi v_m+v_c}{1+\varphi+\varphi v_m-v_c}\varepsilon^* \tag{A.11}$$

$$\varepsilon_y = \frac{(1+v_m)\varphi}{1-v_c+\varphi+\varphi v_m}\left(\varepsilon^* - \frac{v_c\sigma_x}{E_c}\right) \tag{A.12}$$

$$\varepsilon_z = \frac{(1+v_m)\varphi}{1-v_c+\varphi+\varphi v_m}\left(\varepsilon^* - \frac{v_c\sigma_x}{E_c}\right) \tag{A.13}$$

where φ=$E_\mathrm{c}/E_\mathrm{m}$. Applying Eqs. (A.11)-(A.13) to Eqs. (A.5)-(A.7), we can obtain the σ_y and σ_z as functions of ε^*_{ij} and σ_x as follows,

$$\sigma_y = -\frac{E_c}{1-v_c+\varphi+\varphi v_m}\varepsilon^* + \frac{v_c}{1-v_c+\varphi+\varphi v_m}\sigma_x \tag{A.14}$$

$$\sigma_z = -\frac{E_c}{1-v_c+\varphi+\varphi v_m}\varepsilon^* + \frac{v_c}{1-v_c+\varphi+\varphi v_m}\sigma_x \tag{A.15}$$

As both ends of the conductor are fixed, thus

$$u_x(0) = u_x(L) = 0 \tag{A.16}$$

Eq. (A.16) also means that the total integral of strain in the x-direction is zero:

$$\int_0^L \varepsilon_x dx = 0 \tag{A.17}$$

Moreover, based on the 1D equilibrium equation, the σ_x keeps constant along conductor length,

$$\frac{d\sigma_x}{dx} = 0 \;\rightarrow\; \sigma_x = \sigma_0 \tag{A.18}$$

Applying Equations (A.17) and (A.18) to Eq (A.11), we can obtain σ_x as follows,

$$\sigma_x = -\frac{E_c(1+\varphi+\varphi v_m+v_c)}{[(1+v_c)(1-2v_c)+\varphi(1+v_m)]L}\int_0^L \varepsilon^* dx \tag{A.19}$$

Then, using Eq. (A.19) in Eqs. (A.11)-(A.15), following strains and stresses can be determined,

$$\varepsilon_x = \frac{1+\varphi+\varphi v_m+v_c}{1+\varphi+\varphi v_m-v_c}\left(\varepsilon^* - \int_0^L \varepsilon^* dx\right) \tag{A.20}$$

$$\varepsilon_y = \varepsilon_z = \frac{(1+v_m)\varphi}{1-v_c+\varphi+\varphi v_m}\left(\varepsilon^* + \frac{v_c(1+v_c+\varphi+\varphi v_m)}{[(1+v_c)(1-2v_c)+\varphi(1+v_m)]L}\int_0^L \varepsilon^* dx\right) \tag{A.21}$$

$$\sigma_y = \sigma_z = -\frac{E_c}{1-v_c+\varphi+\varphi v_m}\left(\varepsilon^* + \frac{v_c(1+v_c+\varphi+\varphi v_m)}{[(1+v_c)(1-2v_c)+\varphi(1+v_m)]L}\int_0^L \varepsilon^* dx\right) \tag{A.22}$$

Finally, the volumetric strain and hydrostatic stress, based on Eqs. (5) and (19), can be obtained as follows,

$$\theta = \frac{1}{1-v_c+\varphi+\varphi v_m}\left[(1+v_c+3\varphi+3\varphi v_m)\varepsilon^* - \frac{(1+v_c+\varphi+\varphi v_m)^2(1-2v_c)}{[(1+v_c)(1-2v_c)+\varphi(1+v_m)]L}\int_0^L \varepsilon^* dx\right] \tag{A.23}$$

$$\sigma = -\frac{2E_c}{3(1-v_c+\varphi+\varphi v_m)}\left[\varepsilon^* + \frac{(1+v_c+\varphi+\varphi v_m)^2\int_0^L \varepsilon^* dx}{2[(1+v_c)(1-2v_c)+\varphi(1+v_m)]L}\right] \tag{A.24}$$

If the eigenvalue ε^* is diffusion-induced strain, we have,

$$\varepsilon^* = \frac{1}{3}\int_{C_{a0}}^{C_a}(1-f)\frac{dC_a}{C_a} \tag{A.25}$$

Applying Eq. (A.25) to Eqs. (A.23) and (A.24), we can obtain the following equations,

$$\theta = \frac{1}{3(1-v_c+\varphi+\varphi v_m)}\left[(1+v_c+3\varphi+3\varphi v_m)\int_{C_{a0}}^{C_a}(1-f)\frac{dC_a}{C_a} - \frac{(1+v_c+\varphi+\varphi v_m)^2(1-2v_c)}{[(1+v_c)(1-2v_c)+\varphi(1+v_m)]L}\int_0^L\int_{C_{a0}}^{C_a}(1-f)\frac{dC_a}{C_a}dx\right] \tag{A.26}$$

$$\sigma = -\frac{2E_c}{9(1-v_c+\varphi+\varphi v_m)}\left[\int_{C_{a0}}^{C_a}\frac{1-f(C_a)}{C_a}dC_a + \frac{(1+v_c+\varphi+\varphi v_m)^2\int_0^L\int_{C_{a0}}^{C_a}\frac{1-f(C_a)}{C_a}dC_a dx}{2[(1+v_c)(1-2v_c)+\varphi(1+v_m)]L}\right] \tag{A.27}$$

Above Eqs. (A.26) and (A.27) are used in Eq. (3) to obtain the Eq. (32).

Appendix B. Steady state solution and threshold product

Based on Eq. (34), the steady state equation for an un-passivated conductor is

$$-\frac{Z^* e\rho j}{k_B T}\frac{\partial C_a}{\partial x} + \frac{\partial^2 C_a}{\partial x^2} = 0 \tag{B.1}$$

Solving this equation, we can obtain the following equation,

$$\ln\left(\frac{C_a|_{x=0}}{C_a|_{x=L}}\right) = -\frac{Z^* e\rho jL}{k_B T} \tag{B.2}$$

where $C_a|_{x=0}$ is the atomic concentration at cathode (x=0), and $C_a|_{x=L}$ is the atomic concentration at anode (x=L). In the Blech structure, when the atomic concentration at the cathode decreases to critical value, EM failure occurs due to void formation,

$$C_a|_{x=0} = C_{\mathrm{a,critical}} \tag{B.3}$$

As an example shown in Fig. B, in Blech structure, the magnitude of atomic concentration variation at the cathode is same to that at the anode.

Thus, when $C_a|_{x=0}$ reaches $C_{\mathrm{a,crictial}}$, the atomic concentration at anode is

$$C_a|_{x=L} = C_{\mathrm{a0}} + \left(C_{\mathrm{a0}} - C_{\mathrm{a,critical}}\right) = 2C_{\mathrm{a0}} - C_{\mathrm{a,critical}} \tag{B.4}$$

Applying Eqs. (B.3) and (B.4) to Eq. (B.2), we can obtain the threshold product $(jL)_{\mathrm{c}}$ in un-passivated configurations as follows,

$$(jL)_c\big|_{\mathrm{un-passivated}} = \frac{k_B T}{Z^* e\rho}\ln\left(\frac{2C_{\mathrm{a0}}}{C_{\mathrm{a,critcial}}} - 1\right) \tag{B.5}$$

For passivated condition, the steady-state equation is

$$-\frac{Z^* e\rho j}{k_B T}\frac{\partial C_a}{\partial x} + \frac{\partial^2 C_a}{\partial x^2} + \frac{2E_c\Omega}{9(1-v_c+\varphi+\varphi v_m)k_B T}\left[(1-f)\frac{\partial^2 C_a}{\partial x^2} - \frac{\partial f}{\partial C_a}\left(\frac{\partial C_a}{\partial x}\right)^2\right] = 0 \tag{B.6}$$

Solving this equation, we can obtain the following equation,

$$\left[1+\frac{2E_c(1-f)}{9[1-\nu_c+\varphi+\varphi\nu_m]}\frac{\Omega}{k_BT}\right]\ln\left(\frac{C_a|_{x=0}}{C_a|_{x=L}}\right)=-\frac{Z^*e\rho jL_c}{k_BT} \tag{B.7}$$

Applying Eqs. (B.3) and (B.4) to Eq. (B.5), the threshold product $(jL)_c$ in passivated condition can be obtained,

$$(jL)_c\big|_{\text{passivated}}=\frac{k_BT}{Z^*e\rho}\left[1+\frac{2E_c(1-f)\Omega}{9[1-\nu_c+(1+\nu_m)\varphi]k_BT}\right]\ln\left(\frac{2C_{a0}}{C_{a,critcial}}-1\right) \tag{B.8}$$

Appendix C. Determination of $C_{a,critical}$ and D_a

Based on Eq. (B.5), the critical atomic concentration can be obtained vis following equation,

$$\frac{C_{a,\text{critical}}}{C_{a0}}=2\left[\exp\left[\frac{Z^*e\rho(jL)_c}{2k_BT}\right]+1\right]^{-1} \tag{C.1}$$

Eq. (C.1) is the same as Eq. (40). Using the material properties shown in Table 2, e.g., Z^*=1.1, e=1.6 × 10^{-19} C, ρ=2.88 × 10^{-8} Ohm•m, k_B=1.38 × 10^{-23} J/K, T=525 K, and the experimentally determined threshold product, 1000 A/cm for non-annealed Al and 1500 A/cm for annealed Al, then we can obtained that the normalized critical atomic concentrations are 0.965 for annealed Al and 0.949 for annealed Al.

Furthermore, based on experimental results, the drift velocity V_{drift} is 0.0608 ± 0.005 nm/s for 100 μm Al without annealing. Solving Eqs. (24-26)), we can obtain the numerical results for the distributions of C_a, dC_a/dx, and d^2C_a/dx^2 in 100 μm Al without annealing at the moment of EM failure occurring, as shown in Fig. C.

Thus, we can obtain

$$\left.\frac{C_a}{C_a}\right|_{\substack{x=0\\ t=t(\text{failure})}}=0.965 \tag{C.2}$$

$$\left.\frac{\partial C_a}{C_{a0}\partial x}\right|_{\substack{x=0\\ t=t(\text{failure})}}=3.1\ \times 10^4\ m^{-1} \tag{C.3}$$

$$\left.\frac{\partial^2 C_a}{C_a\partial x^2}\right|_{\substack{x=0\\ t=t(\text{failure})}}=-5\ \times 10^{10}\ m^{-2} \tag{C.4}$$

Using the material properties shown in Table 2, e.g. Z^*=1.1, e=1.6 × 10^{-19} C, ρ=2.3 × 10^{-8} Ohm•m, k_B=1.38 × 10^{-23} J/K, T=525 K, Ω=1/C_{a0}, L=100 μm, and the numerical results shown in Eqs. (C.2-C.4), then we can obtain the atomic diffusivity for Al without annealing as 8.5 × 10^{-15} m^2/s by using Eq. (46). Similarly, we can obtain that the atomic diffusivity for Al with annealing is 4.8 × 10^{-15} m^2/s.

References

Black, J.R., 1967. Mass transport of aluminum by momentum exchange with conducting electrons. In: 6th Annual Reliability Physics Symposium (IEEE). IEEE, pp. 148–159.

Black, J.R., 1969. Electromigration—A brief survey and some recent results. IEEE Trans. Electron Devices 16, 338–347.

Blech, I., 1998. Diffusional back flows during electromigration. Acta Mater. 46, 3717–3723.

Blech, I., Herring, C., 1976. Stress generation by electromigration. Appl. Phys. Lett. 29, 131–133.

Blech, I.A., 1976. Electromigration in thin aluminum films on titanium nitride. J. Appl. Phys. 47, 1203–1208.

Børgesen, P., Korhonen, M., Brown, D., Li, C.Y., 1992a. Stress-induced voiding and electromigration. In: AIP Conference Proceedings. American Institute of Physics, pp. 219–235.

Børgesen, P., Korhonen, M., Li, C.-Y., 1992b. Stress and current induced voiding in passivated metal lines. Thin. Solid. Films 220, 8–13.

Ceric, H., de Orio, R.L., Cervenka, J., Selberherr, S., 2008. A comprehensive TCAD approach for assessing electromigration reliability of modern interconnects. IEEE Trans. Device Mater. Reliability 9, 9–19.

Chao, B., Chae, S.-H., Zhang, X., Lu, K.-H., Ding, M., Im, J., Ho, P.S., 2006. Electromigration enhanced intermetallic growth and void formation in Pb-free solder joints. J. Appl. Phys. 100, 084909.

Chen, C., Hsiao, H.-Y., Chang, Y.-W., Ouyang, F., Tu, K.-N., 2012. Thermomigration in solder joints. Mater. Sci. Eng. 73, 85–100.

Chen, C., Tong, H., Tu, K.-N., 2010. Electromigration and thermomigration in Pb-free flip-chip solder joints. Annu. Rev. Mater. Res. 40, 531–555.

Cho, J., Thompson, C., 1989. Grain size dependence of electromigration-induced failures in narrow interconnects. Appl. Phys. Lett. 54, 2577–2579.

Clement, J., 1992. Vacancy supersaturation model for electromigration failure under dc and pulsed dc stress. MRS Online Proc. Library 265.

Clement, J., 1997. Reliability analysis for encapsulated interconnect lines under dc and pulsed dc current using a continuum electromigration transport model. J. Appl. Phys. 82, 5991–6000.

Clement, J., Thompson, C., 1995. Modeling electromigration-induced stress evolution in confined metal lines. J. Appl. Phys. 78, 900–904.

Cui, Z., 2021. Multi-physics driven electromigration study: multi-scale modeling and experiment. Ph.D. dissertation. Delft University of Technology.

Cui, Z., Fan, X., Zhang, G., 2019. General coupling model for electromigration and one-dimensional numerical solutions. J. Appl. Phys. 125, 105101.

Cui, Z., Fan, X., Zhang, Y., Vollebregt, S., Fan, J., Zhang, G.Q., 2023. Coupling model of electromigration and experimental verification – part II: impact of thermomigration. Processing Paper.
Cui, Z., Fan, X., Zhang, G., 2020. Implementation of general coupling model of electromigration in ANSYS. 2020 IEEE 70th Electronic Components and Technology Conference (ECTC). IEEE, pp. 1632–1637.
Cui, Z., Fan, X., Zhang, G., 2021. Molecular dynamic study for concentration-dependent volume relaxation of vacancy. Microelectron. Reliab. 120, 114127.
Dandu, P., Fan, X., 2011. Assessment of current density singularity in electromigration of solder bumps. In: 2011 IEEE 61st Electronic Components and Technology Conference (ECTC). IEEE, pp. 2192–2196.
Dandu, P., Fan, X., Liu, Y., 2010. Some remarks on finite element modeling of electromigration in solder joints. In: 2010 Proceedings 60th Electronic Components and Technology Conference (ECTC). IEEE, pp. 396–402.
Dang;, B., Oril;, Y., Talocia;, S.G., 2021. Heterogeneous integration roadmap. In: IEEE Electronics Packaging Society.
Gambino, J.P., Lee, T.C., Chen, F., Sullivan, T.D., 2009. Reliability challenges for advanced copper interconnects: electromigration and time-dependent dielectric breakdown (TDDB). In: 2009 16th IEEE International Symposium on the Physical and Failure Analysis of Integrated Circuits. IEEE, pp. 677–684.
Gan, C., Thompson, C., Pey, K., Choi, W., Tay, H., Yu, B., Radhakrishnan, M., 2001. Effect of current direction on the lifetime of different levels of Cu dual-damascene metallization. Appl. Phys. Lett. 79, 4592–4594.
Gardner, D.S., Meindl, J.D., Saraswat, K.C., 1987. Interconnection and electromigration scaling theory. IEEE Trans. Electron Devices 34, 633–643.
Garikipati, K., Bassman, L., Deal, M., 2001. A lattice-based micromechanical continuum formulation for stress-driven mass transport in polycrystalline solids. J. Mech. Phys. Solids 49, 1209–1237.
Giroux, F., Gounelle, C., Mortini, P., Ghibaudo, G., 1995. Wafer-level electromigration tests on NIST and SWEAT structures. In: Proceedings International Conference on Microelectronic Test Structures. IEEE, pp. 229–232.
Giroux, F., Gounelle, C., Vialle, N., Mortini, P., Ghibaudo, G., 1994. Current and temperature distribution impact on electromigration failure location in SWEAT structure. In: Proceedings of 1994 IEEE International Conference on Microelectronic Test Structures. IEEE, pp. 214–217.
Gleixner, R., Clemens, B., Nix, W., 1997. Void nucleation in passivated interconnect lines: effects of site geometries, interfaces, and interface flaws. J. Mater. Res. 12, 2081–2090.
He, J., Suo, Z., Marieb, T., Maiz, J., 2004. Electromigration lifetime and critical void volume. Appl. Phys. Lett. 85, 4639–4641.
Hemmert, R., Costa, M., 1991. Electromigration-induced compressive stresses in encapsulated thin-film conductors. In: IEEE Proc. Int. Reliab. Phys. Symp, pp. 64–69.
Ho, P.S., Kwok, T., 1989. Electromigration in metals. Rep. Prog. Phys. 52, 301.
Hu, C.-K., Gignac, L., Lian, G., Cabral, C., Motoyama, K., Shobha, H., Demarest, J., Ostrovski, Y., Breslin, C., Ali, M., 2018a. Mechanisms of electromigration damage in Cu interconnects. In: 2018 IEEE International Electron Devices Meeting (IEDM). IEEE, 5.2. 1-5.2. 4.
Hu, C.-K., Kelly, J., Huang, H., Motoyama, K., Shobha, H., Ostrovski, Y., Chen, J.H., Patlolla, R., Peethala, B., Adusumilli, P., 2018b. Future on-chip interconnect metallization and electromigration. In: 2018 IEEE International Reliability Physics Symposium (IRPS). IEEE, pp. 1–6, 4F. 1-1-4F.
Hu, C.-K., Luther, B., 1995. Electromigration in two-level interconnects of Cu and Al alloys. Mater. Chem. Phys. 41, 1–7.
Hu, C.-K., Rosenberg, R., Rathore, H., Nguyen, D., Agarwala, B., 1999. Scaling effect on electromigration in on-chip Cu wiring. In: Proceedings of the IEEE 1999 International Interconnect Technology Conference (Cat. No. 99EX247). IEEE, pp. 267–269.
Hu, C.K., Small, M., Ho, P., 1993. Electromigration in Al (Cu) two-level structures: effect of Cu and kinetics of damage formation. J. Appl. Phys. 74, 969–978.
Jeong, W., Kim, K., Kim, Y., Lee, W., Reddy, P., 2014. Characterization of nanoscale temperature fields during electromigration of nanowires. Sci. Rep. 4, 1–6.
Jonggook, K., Tyree, V., Crowell, C., 1999. Temperature gradient effects in electromigration using an extended transition probability model and temperature gradient free tests. I. Transition probability model. In: 1999 IEEE International Integrated Reliability Workshop Final Report (Cat. No. 99TH8460). IEEE, pp. 24–40.
Kijkanjanapaiboon, K., 2017. Modeling of Electromigration and Lock-In Thermography in Microelectronics and Microelectronics Packaging. Ph.D. dissertation. Lamar University.
Kirchheim, R., 1992. Stress and electromigration in Al-lines of integrated circuits. Acta Metall. Mater. 40, 309–323.
Kirchheim, R., Kaeber, U., 1991. Atomistic and computer modeling of metallization failure of integrated circuits by electromigration. J. Appl. Phys. 70, 172–181.
Korhonen, M., Børgesen, P., Tu, K.-N., Li, C.Y., 1993. Stress evolution due to electromigration in confined metal lines. J. Appl. Phys. 73, 3790–3799.
Kozlova, T., Rudneva, M., Zandbergen, H.W., 2013. In situ TEM and STEM studies of reversible electromigration in thin palladium–platinum bridges. Nanotechnology 24, 505708.
Kraatz, M., Gall, M., Zschech, E., Schmeisser, D., Ho, P.S., 2016. A model for statistical electromigration simulation with dependence on capping layer and Cu microstructure in two dimensions. Comput. Mater. Sci. 120, 29–35.
Kraft, O., Arzt, E., 1998. Current density and line width effects in electromigration: a new damage-based lifetime model. Acta Mater. 46, 3733–3743.
Lau, J.H., 2022. Recent advances and trends in advanced packaging. IEEE Trans. Comp., Pack. Manuf. Technol. 12, 228–252.
Li, S., Sellers, M.S., Basaran, C., Schultz, A.J., Kofke, D.A., 2009. Lattice strain due to an atomic vacancy. Int. J. Mol. Sci. 10, 2798–2808.
Liang, C.-L., Lin, Y.-S., Kao, C.-L., Tarng, D., Wang, S.-B., Hung, Y.-C., Lin, G.-T., Lin, K.-L., 2020. Electromigration reliability of advanced high-density fan-out packaging with fine-pitch 2-/2-μm L/S Cu redistribution lines. IEEE Trans. Comp., Pack. Manuf. Technol. 10, 1438–1445.
Lin, M., Basaran, C., 2005. Electromigration induced stress analysis using fully coupled mechanical–diffusion equations with non-linear material properties. Comput. Mater. Sci. 34, 82–98.
Lin, Y., Hu, Y., Tsai, C., Kao, C., Tu, K.-N., 2005. In situ observation of the void formation-and-propagation mechanism in solder joints under current-stressing. Acta Mater. 53, 2029–2035.
Liu, P., 2017. Fundamentals of Electromigration in Interconnects of 3D Packaging, 3D Microelectronic Packaging. Springer, pp. 223–244.
Lloyd, J., 1982. Electromigration in Al-Cu thin films with polyimide passivation. Thin. Solid. Films 91, 175–182.
Lloyd, J., 1999. Electromigration and mechanical stress. Microelectron. Eng. 49, 51–64.
Lloyd, J., Smith, P., 1983. The effect of passivation thickness on the electromigration lifetime of Al/Cu thin film conductors. J. Vacuum Sci. Technol. A 1, 455–458.
Ouyang, F.-Y., Kao, C.-L., 2011. In situ observation of thermomigration of Sn atoms to the hot end of 96.5 Sn-3Ag-0.5 Cu flip chip solder joints. J. Appl. Phys. 110, 123525.
Pharr, M., Zhao, K., Suo, Z., Ouyang, F.-Y., Liu, P., 2011. Concurrent electromigration and creep in lead-free solder. J. Appl. Phys. 110, 083716.
Proost, J., Delaey, L., D'Haen, J., Maex, K., 2002. Plasticity of electromigration-induced hillocking and its effect on the critical length. J. Appl. Phys. 91, 9108–9115.
Rangaraju, N., Raghuram, T., Krishna, B.V., Rao, K.P., Venugopal, P., 2005. Effect of cryo-rolling and annealing on microstructure and properties of commercially pure aluminium. Mater. Sci. Eng. 398, 246–251.
Rao, P.N., Singh, D., Jayaganthan, R., 2013. Effect of annealing on microstructure and mechanical properties of Al 6061 alloy processed by cryorolling. Mater. Sci. Technol. 29, 76–82.
Root, B.J., Turner, T., 1985. Wafer level electromigration tests for production monitoring. In: 23rd International Reliability Physics Symposium. IEEE, pp. 100–107.
Rzepka, S., Meusel, E., Korhonen, M., Li, C.-Y., 1999. 3-D finite element simulator for migration effects due to various driving forces in interconnect lines, AIP Conference proceedings. Am. Inst. Phys. 150–161.
Sarychev, M., Zhitnikov, Y.V., Borucki, L., Liu, C.-L., Makhviladze, T., 1999. General model for mechanical stress evolution during electromigration. J. Appl. Phys. 86, 3068–3075.
Shatzkes, M., Lloyd, J., 1986. A model for conductor failure considering diffusion concurrently with electromigration resulting in a current exponent of 2. J. Appl. Phys. 59, 3890–3893.
Sukharev, V., Zschech, E., 2004. A model for electromigration-induced degradation mechanisms in dual-inlaid copper interconnects: Effect of interface bonding strength. J. Appl. Phys. 96, 6337–6343.
Sukharev, V., Zschech, E., Nix, W.D., 2007. A model for electromigration-induced degradation mechanisms in dual-inlaid copper interconnects: Effect of microstructure. J. Appl. Phys. 102, 053505.
Suo, Z., 2003. Reliability of interconnect structures. In: Gerberich, W., W.Y. (Eds.), Interfacial and Nanoscale Failure. Elsevier, Amsterdam, pp. 265–324.

Tan, C.M., Roy, A., 2007. Electromigration in ULSI interconnects. Mater. Sci. Eng. 58, 1–75.
Tezaki, A., Mineta, T., Egawa, H., Noguchi, T., 1990. Measurement of three dimensional stress and modeling of stress induced migration failure in aluminium interconnects. In: 28th Annual Proceedings on Reliability Physics Symposium. IEEE, pp. 221–229.
Tong, X., Zhang, H., Li, D., 2015. Effect of annealing treatment on mechanical properties of nanocrystalline α-iron: an atomistic study. Sci. Rep. 5, 1–7.
Tu, K.-N., 2003. Recent advances on electromigration in very-large-scale-integration of interconnects. J. Appl. Phys. 94, 5451–5473.
Tu, K.-N., Liu, Y., Li, M., 2017. Effect of Joule heating and current crowding on electromigration in mobile technology. Appl. Phys. Rev. 4, 011101.
Volin, T., Balluffi, R., 1968. Annealing kinetics of voids and the Self-diffusion coefficient in aluminum. Phys. Status Solidi 25, 163–173.
Wada, T., Sugimoto, M., Ajiki, T., 1987. The influence of passivation and packaging on electromigration. Solid State Electron. 30, 493–496.
Yao, W., Basaran, C., 2013. Computational damage mechanics of electromigration and thermomigration. J. Appl. Phys. 114, 103708.
Yuzuriha, T., Early, S., 1986. Failure mechanisms in a 4 micron pitch 2-layer gold IC metallization process. In: IEEE VLSI MIC Conference, p. 146.
Zhang, G.-Q., Roosmalen, A.V., 2009. More than Moore. Springer.
Zhang, G.-Q., Van Driel, W.D., Fan, X., 2006. Mechanics of Microelectronics. Springer Science & Business Media.
Zhang, G.Q., Roosmalen, V., 2010. More than Moore: Creating High Value Micro/Nanoelectronics Systems. Springer Science & Business Media.
Zhang, L., Wang, P.-C., Liu, X.H., McLaughlin, P.S., Filippi, R., Li, B., Bao, J., 2013. Electromigration extrusion kinetics of Cu interconnects. In: 2013 IEEE International Reliability Physics Symposium (IRPS). IEEE, 2C. 4.1-2C. 4.5.
Zhang, Y., Liu, Y., Liang, L., Fan, X., 2012. The effect of atomic density gradient in electromigration. Int. J. Mater. Struct. Integr. 6, 36–53.
Zhang, Y., 2020. Experimental study on electromigration using Blech structure. Master thesis. Delft University of Technology.
Zhou, X., Yu, X., Jacobson, D., Thompson, G.B., 2019. A molecular dynamics study on stress generation during thin film growth. Appl. Surf. Sci. 469, 537–552.
Zhu, C., Ning, W., Li, H., Zheng, T., Xu, G., Luo, L., 2014. Void control during plating process and thermal annealing of through-mask electroplated copper interconnects. Microelectron. Reliab. 54, 773–777.